Coastal horizontal wind speed gradients in the North Sea based on observations and ERA5 reanalysis data

Beatriz Cañadillas[1,2*], Shuhan Wang[1], Yasmin Ahlert[1], Bughsin' Djath[3], Mares Barekzai[4], Richard Foreman[2] and Astrid Lampert[1]

[1]Institute of Flight Guidance, Technische Universität Braunschweig, Germany
[2]Renewables, UL International GmbH, Germany
[3]Institute of Coastal Systems - Analysis and Modeling, Helmholtz-Zentrum Hereon, Geesthacht, Germany
[4]Karlsruhe Institute of Technology, Garmisch-Partenkirchen, Germany

Abstract

The transition from land to sea affects the wind field in coastal regions. From the perspective of near-coastal offshore wind farms, the coastal transition complicates the task of energy resource assessment by, for example, introducing non-homogeneity into the free wind field. To help elucidate the matter, we quantify the average horizontal wind speed gradients at progressively increasing distances from the German coast using two years of hourly ERA5 reanalysis data, and further describe the dependence of wind speed gradients on the measurement height, atmospheric stability, and season. A vertical wind lidar located on Norderney Island near the German mainland acts as our observational reference for the ERA5 data, where a good agreement ($R^2 = 0.93$) is found despite the relatively coarse ERA5 data resolution. Interestingly, the comparison of lidar data with the higher-resolution Weather Research and Forecasting (WRF) mesoscale model yields good but relatively weaker agreement ($R^2 = 0.85$). The ERA5 data reveal that, for flow over the North Sea originating from the German mainland from the south, the wind speed at 10 m (110 m) above sea level increases by 30 % (20 %) some 80 km from the coast on average, and by 5 % at larger heights. An increased stratification increases the horizontal wind speed gradient at 10 m above sea level but decreases it at 110 m. Case studies using satellite and flight measurements are first analyzed to help reveal some of the underlying mechanisms governing horizontal wind speed gradients, including cases of decreasing wind speed with increasing distance from the coast, in which stable flow of warm air over the colder sea leads to an overall deceleration of the flow. The accuracy of offshore resource assessment appears to profit from utilising the horizontal wind speed gradient information contained in ERA5 reanalysis data.

Keywords: coastal wind speed gradients, ERA reanalysis, offshore, wind energy

1 Introduction

The development of offshore wind energy has the advantage of more favourable wind resources compared with over land, namely, the higher wind speed and lower turbulence resulting from the lower surface roughness of water compared with that found onshore. Most offshore wind farms are still located in relative proximity to the coastline mostly due to the increasing costs of the wind turbine foundation with water depth, which increases with distance from the coast, as well as the connection costs to the electricity grid. In the case of the North Sea, at present, a significant number of wind turbines are currently located at a distance of between 15 km (Borkum Riffgat wind farm) and 200 km for southerly directions (Schulz-Stellenfleth et al., 2022) from the European mainland, while worldwide most of the offshore wind farms operating to date are deployed within 20 km to the shoreline at a maximum average water depth of 30 m (Díaz and Guedes Soares, 2020). Therefore,

the need for understanding and a quantification of the coastal flow complexities are highly relevant for wind energy.

The surface discontinuity at the coastline as the flow moves from the rougher land surface to over the smoother sea surface, the influence of the along-shore topography, and thermal gradients, which are influenced by the diurnal and annual cycle of solar radiation, are some of the principal complexities affecting land–sea flows (Barthelmie et al., 2007). Early studies by Smedman and co-authors (e.g. Smedman, 1991; Smedman et al., 1996) as well as the work of Barthelmie and co-authors (e.g. Barthelmie et al., 1996b; Pryor and Barthelmie, 1998; Barthelmie, 1999; Barthelmie, 2001; Barthelmie et al., 2007) have been very valuable for understanding the importance of these complexities and how they influence the flows in the coastal areas of the Baltic and North Sea, respectively. In Schulz-Stellenfleth et al. (2022), an up-to-date overview of the flow complexities in coastal areas, including low-level jets (LLJs), with a focus on the area of the German Bight in the North Sea, is given.

*Corresponding author: Beatriz Cañadillas (b.canadillas@tu-braunschweig.de, beatriz.canadillas@ul.com)

In the simplest land–sea flow scenario involving only an instant reduction in the roughness length z_0 over water while neglecting thermal effects, early investigations give some estimates of the expected increase in wind speed for increasing fetch from the coast, as well as the distance offshore where the wind speed reaches an 'equilibrium' and ceases to increase significantly. Here equilibrium is given due to a balance between surface friction, large scale pressure gradients, and the Coriolis force. For example, the two-dimensional model of TAYLOR (1969) suggests that at 10-m altitude the wind speed of $10\,\mathrm{m\,s^{-1}}$ at the coast increases by approximately $30\,\%$ at $60\,\mathrm{km}$ downstream and has not reached equilibrium even at this distance. BARTHELMIE et al. (1996a) investigated mean vertical wind speed profiles from on- and offshore tower measurements in the Baltic Sea separated by a few kilometres showing a wind speed increase from land to sea of about $25\,\%$ at a height of $7\,\mathrm{m}$, but the effect is less pronounced with increasing height above the surface and amounting to at most $5\,\%$ at a height of $38\,\mathrm{m}$ at these relatively short fetches. Such a height dependence was recently emphasized in SHIMADA et al. (2018) who found the speed-up disappearing at heights of $130\,\mathrm{m}$ above the sea in their lidar measurements for a range of short fetches at a Japanese coastal location. For their results at a height of $50\,\mathrm{m}$, a wind speed increase of approximately $20\,\%$ was recorded by their two lidars up to fetches of $5\,\mathrm{km}$.

The dependence of the wind speed gradients on atmospheric stability was also suspected early on. PRYOR and BARTHELMIE (1998) presented wind speed distributions from the Baltic Sea and showed that at a distance of 1.2–$1.7\,\mathrm{km}$ from the coast, up to a height of $20\,\mathrm{m}$ above the surface, differences in wind speed distributions from onshore and offshore masts are statistically significant for flow moving offshore under all stability conditions.

AHSBAHS et al. (2018) showed that wind speed maps retrieved from synthetic aperture radar (SAR) images can be used to predict the spatial wind speed variability at a potential wind farm site before construction begins and to partially determine the cumulative effects of coastal wind speed gradients and wake effects. It was found that wind speeds retrieved from SAR correlate well with the SCADA-derived wind speeds for the turbines at Anholt wind farm with RMSEs of 2.23 and $2.12\,\mathrm{m\,s^{-1}}$ for comparisons upstream and downstream of the wind farm, respectively. DJATH et al. (2022) also used SAR images to investigate 10-m wind speed gradients far out to the North Sea and presented one particular case in very stable offshore conditions showing an increase in wind speed out to some $150\,\mathrm{km}$ offshore, with a corresponding wind speed increase of $180\,\%$. On average, however, the 10-m wind speed is found to increase by roughly $20\,\%$ beyond $50\,\mathrm{km}$ offshore. In general, the SAR data reveal that stable offshore situations lead to a higher wind speed increase by up to a factor of two compared with unstable offshore conditions.

A further complexity highlighted in DJATH et al. (2022) is that the land–sea horizontal wind speed gradients may even decrease with increasing distance from the coast in a minority of cases. Such an event was measured with flight measurements in the Baltic Sea and investigated by KÄLLSTRAND et al. (2000) which they attribute to the slow growth of a stable internal boundary layer out to sea. The investigation by LAPWORTH (2005) concerning the offshore diurnal cycle for flow from land to sea also revealed both increasing and decreasing wind speed with fetch depending on the land–sea temperature gradient.

It is these effects, the influence of stability on wind speed gradients and whether one detects a positive or negative gradient, that we wish to quantify here with a view to providing information for the ongoing development of the offshore wind sector.

For this purpose, one can analyze measurements but, due to the relative lack of such continuous and frequent sources of data (e.g. SAR data, HASAGER et al., 2011; LI and LEHNER, 2013; AHSBAHS et al., 2020; DJATH et al., 2018; DJATH and SCHULZ-STELLENFLETH, 2019; DJATH et al., 2022), models can be a good alternative, even if they are perhaps not as accurate. For instance, reanalysis models, weather models which assimilate observations from the historical record, are often used in wind energy at locations where few observations are available or are not comprehensive enough for assessing the long-term wind regime at a given site (e.g. DRAXL et al., 2015; SANTOS et al., 2019; SHAMSHIRBAND et al., 2020; THOMAS et al., 2021), at both offshore and onshore locations. Reanalyses are usually published regularly, and are frequently used for studies on wind power generation potential due to their global coverage and the length of time they cover. For example, ZHENG et al. (2018) classified the world's offshore wind energy resources using reanalysis data. SOARES et al. (2020) used reanalysis data to perform a global quantitative characterization of offshore wind power density over the economic exclusive zones at annual and seasonal scales. Reanalysis products can be used also to identify commonly occurring calm weather periods for construction and maintenance periods (SHERIDAN et al., 2021). PODEIN et al. (2022) used reanalysis data to reconstruct offshore wind speed based on the linear correlation between measurements and reanalysis. In addition, reanalysis models provide input boundary conditions for higher resolution wind models (e.g. HAHMANN et al., 2020; DÖRENKÄMPER et al., 2020). Despite the obvious utility of reanalysis data for a range of wind energy applications, it is still important to assess the accuracy of such datasets, particularly in difficult flow situations, such as in complex terrain or in the land–sea flows considered here. MERRA2 reanalysis data and measured offshore mast data (at $50\,\mathrm{m}$ above mean sea level) were analysed in SOLER-BIENTZ and WATSON (2016) to determine patterns in wind speed variation and how they change as a function of the distance from the coast (up to $150\,\mathrm{km}$). It was found that the variations of the seasonal cycles were almost independent of the distance to the nearest shore and that they are an order of magnitude larger than the variations of

Meteorol. Z. (Contrib. Atm. Sci.)
Early Access Article, 2023

B. Cañadillas et al.: Coastal horizontal wind speed gradients

3

the diurnal cycles. It was concluded that the diurnal variations decreased to less than a half for places located more than 100 km from the nearest shore and that the data from the MERRA2 reanalysis grid points give an under-prediction of the average values of wind speed for both the diurnal and seasonal cycles. In SANTOS et al. (2019), three reanalysis products (namely MERRA-2, ERA-Interim and ERA5) were validated using mast data in northeastern Brazil, with ERA5 showing the highest correlation for a nine-year period (0.95) at 100 m altitude for monthly means where the wind speed observations were systematically underestimated. PRONK et al. (2022) used one year of lidar data in simple terrain and offshore sites to evaluate the performance of the Weather Research and Forecasting (WRF) model and the ERA5 reanalysis product, with a focus on characterizing the wind resource. The ERA5 reanalysis data have a significant negative bias ($\approx 1\,\mathrm{m\,s^{-1}}$) at both locations, with a larger bias at the onshore site. The WRF predicted wind speed profiles show a negative bias ($-0.5\,\mathrm{m\,s^{-1}}$) offshore and a slight positive bias ($0.5\,\mathrm{m\,s^{-1}}$) at the onshore site. In addition, ERA5 is found to outperform the WRF model in terms of centred root-mean-square error (RMSE) and correlation coefficient R for the land and sea cases under all atmospheric stability conditions. In the offshore case, the WRF model tends to overpredict the amplitude of the diurnal wind speed cycle. OLAUSON (2018) showed, through a comprehensive evaluation of wind speed at turbine height in Sweden, that ERA5 performs better than MERRA-2 (a reanalysis previously used in the wind industry) in all aspects analyzed (correlations are higher, errors are on average about 20 % lower, and the distributions of both hourly data and changes in hourly data are more similar to those of the measurements). In JOURDIER (2020), an analysis of several global reanalysis data and high resolution data were conducted over France. Despite the lower resolution compared to the regional models, ERA5 generally performs well, but yields large negative biases over mountainous areas. In GUALTIERI (2021), ERA5 reanalyses data were assessed with respect to observations from six tall towers installed over very heterogeneous sites around the world. A larger discrepancy in the comparison of ERA5 with in situ wind data was found at sites with high variation in topography and, in particular, land use. However, results were acceptable at the FINO3 (Baltic Sea) offshore platform for wind speed (bias within 1 %, $R = 0.95$–0.96) and at the flat and sea-level site of Cabauw (Netherlands) for wind speed (bias within 7 %, $R = 0.93$–0.94).

SHERIDAN et al. (2021) evaluated four commonly used reanalysis models in the wind energy industry using two lidar buoys, located on the USA East Coast, in order to analyze their ability to capture offshore hub height wind speed. Overall, ERA5 is the best reanalysis model for capturing the offshore hub height wind resource in terms of optimizing bias ($-0.5\,\mathrm{m\,s^{-1}}$), RMSE ($2\,\mathrm{m s^{-1}}$), and correlation ($R \approx 0.9$). However, a major drawback of reanalysis products is the low spatial and temporal resolution compared to high-resolution regional or mesoscale models, which are supposed to provide a more accurate estimate of the wind resource, as they can capture regional-scale features (coastal jets and breezes, land–sea and topographic circulations).

The New European Wind Atlas (NEWA) and ERA5 reanalysis data were compared at several offshore sites in MEYER and GOTTSCHALL (2022). On average, NEWA showed to be more accurate (lower bias) but less precise (lower correlation coefficients) in terms of predicting mean wind speed compared to ERA5. Extreme wind speeds were underestimated by both datasets. Altogether, ERA5 is a good option when using long-term MCP (Measure-Correlate-Predict) methods.

The objective of this study is to evaluate horizontal wind speed gradients as a function of fetch length (distance to the coast) by means of ERA5 reanalysis data, focusing on southerly winds (for flow from land towards the sea) occurring in part of the German Bight. In particular, the influence of atmospheric stability on horizontal wind speed gradients is examined, including cases of both positive and negative gradients for different stability. Because of the uncertainty in the accuracy of the ERA5 data due to its supposed coarse horizontal resolution for coastal environments, we compare the ERA5 data with observations at two locations (a coastal and an offshore site) and with a mesoscale model whose set-up is based on the New European Wind Atlas (NEWA), which is a downscaling of the ERA5 reanalysis to 2 km using the WRF model (e.g. HAHMANN et al., 2020; DÖRENKÄMPER et al., 2020). The WRF simulations enable the assessment of whether a finer spatial resolution and a more comprehensive physics could outperform ERA5 data (PRONK et al., 2022).

The paper is structured as follows: Section 2 provides an overview of the site. Section 3 introduces the data sets and methods used in the analysis, including a brief comparison between model and observational data. Two data sources (SAR and aircraft) are used in Section 4 to help reveal the underlying processes involved in the generation of the wind speed gradients, particularly with regard to the vertical temperature profiles both on- and offshore. The horizontal wind speed gradients in the North Sea are presented in Section 5. Finally our discussion and conclusions are given in Section 6.

2 Study area

This study focuses on the southern coastal area of the German North Sea, located between the island of Norderney (coast) and 139 km to the north (offshore). The water depth varies between 0 m (Wadden Sea periodically falling dry) and 50 m at locations further offshore (Figure 1). At Norderney Island a vertical wind lidar was installed (53° 42.75′ N, 07° 09.13′ E) at the German Weather Service (DWD) site and operated by the company UL International. The data is considered here for comparison and as a reference from 1 April 2020
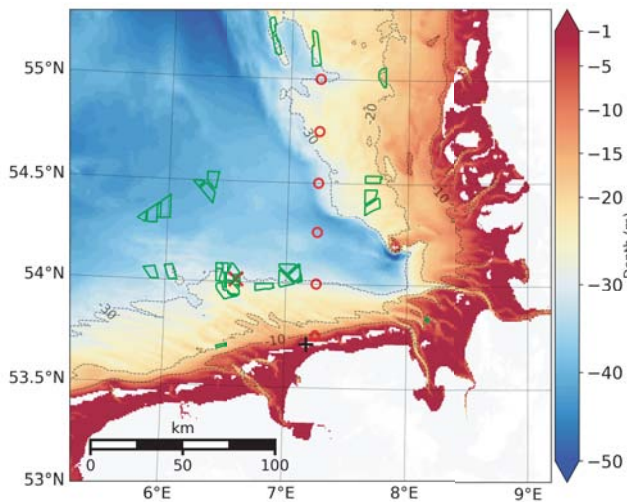
Figure 1: Location of the study area and its bathymetry (colour coded) with the position of the lidar at Norderney Island and the FINO1 mast are marked with a black plus and red cross symbols, respectively. The areas of wind farms currently in operation are denoted by green polygons. Bathymetry data have been obtained from GEBCO COMPILATION GROUP (2020). The superimposed red circles characterise the ERA5 grids selected for the statistical analysis.

3   Data and methods

This section presents the observations used in the comparison at two sites, at the coast (Norderney), and at an offshore site (FINO1 platform), and the reanalysis used for the statistical analysis (ERA5) as the primary data source. Additionally, mesoscale model data are only used in this study to assess whether a large bias is to be anticipated in the reanalysis data, as these models are expected to be more accurate than reanalysis products in the characterisation of wind resources due to their finer spatial resolution and more comprehensive physical properties, as outlined in KALVERLA et al. (2019) and PRONK et al. (2022). Furthermore, two additional observations, namely synthetic aperture radar (SAR) images and airborne data, are used as case studies to aid understanding the horizontal wind speed gradients at the coast based on reanalysis data. It is worth mentioning that these particular observations have not been assimilated into the reanalyses or mesoscale models used in this study.

3.1   Data description

3.1.1   ERA5 reanalysis

ERA5 HRES (High Resolution) (HERSBACH et al., 2020) is an hourly global reanalysis dataset containing a large number of atmospheric, land, and oceanic climate variables from 1979 to near real time (with 2–3 months delay). It covers the entire Earth using 137 vertical levels ranging from the surface up to a height of about 80 km. The ERA5 atmospheric model is coupled with a land surface model and a wave model and is the latest reanalysis dataset from the European Centre for Medium-range Weather Forecasts (ECMWF). ERA5 outputs are generated by the current version of the Integrated Forecasting System (IFS Cycle 41r2) and as its predecessor (ERA-Interim) makes use of the four-dimensional variational analysis (4D-Var) assimilation system (DEE et al., 2011) with a 12-h temporal window. The data are freely available at the horizontal grid spacing of approximately 31 km. Whenever and wherever available, historical observations, including satellite as well as in situ data, such as synoptic ground-based observations, METeorological Aerodrome Reports (METAR), radiosounding, wind profiler, radar, aircraft, buoy, and ship data are assimilated into the ERA reanalysis product.

3.1.2   Mesoscale dataset: WRF

The mesoscale simulations were performed using the WRF model (Version 4.2.1) developed by the National Center of Atmospheric Research (SKAMAROCK et al., 2019). The model predicts the horizontal and vertical wind components, potential temperature, geopotential and surface pressure of dry air as well as water vapor and cloud water. The WRF model is well established and widely applied in the wind energy community (HAHMANN et al., 2020; KIBONA, 2020) and in recent years also for wind farm wake analyses (SIEDERSLEBEN et al., 2018; PRYOR et al., 2019). Simulations of three nested domains centred around the German Bight area were performed, with a resolution of 18 km, 6 km and 2 km. This nested approach reduces the number of grid points and therefore computational cost. The boundary conditions for the atmospheric variables were prescribed by the ERA5 dataset (HERSBACH et al., 2020), with a spatial resolution of $0.25° × 0.25°$ ($≈ 30$ km) and a temporal resolution of 6 h. Furthermore, the OSTIA dataset for the sea surface variables (DONLON et al., 2012) is applied, providing a high spatial resolution of $0.05° × 0.05°$ ($≈ 6$ km) as daily averages, which are interpolated in 6 hour intervals. The used WRF version 4.2.1 accounts for the turbulent-kinetic-energy advection bug that was recently discovered (ARCHER et al., 2020). Finally, no wind farm parameterization is included in the simulations as well as no data assimilation. A summary of the most important model configuration decisions can be found in Table 1.

to 31 March 2021. The island of Norderney (extension 14 km × 2.5 km) is one of the East Frisian Islands and lies only a few kilometres from the German North Sea coast. The DWD site is located at an altitude of 7 m above sea level. No obstacles interfere with the lidar measurement. For southerly wind directions, the coastal transition strongly influences the development of wind speed above the North Sea.

Table 1: Relevant parameters of the mesoscale model set-up. The references for the different schemes and models are summarized in WRF Users Page (2020).

Parameter	Setting
WRF model version	4.2.1
Planetary Boundary Layer (BLH) scheme	MYNN level 2.5
Land use data	MODIS
Surface layer scheme	MYNN
Microphysics scheme	WRF Single-Moment 5-class
Shortwave and longwave radiation	RRTMG
Atmospheric boundary conditions	ERA5
Sea surface conditions	OSTIA
Horizontal resolution	18 km, 6 km, 2 km
Vertical resolution	60 eta-levels
Nudging	grid nudging above BLH
Model output interval	10 min
Nesting	one-way
Land surface model	Unified Noah Land Surface Model
Simulation duration	240 (+24 spin-up) hours

3.1.3 Wind lidar

A profiling ground-based wind lidar system, Windcube WLS8, developed by Leosphere (now Vaisala), was installed at the German coast (53° 42.75′ N, 7° 9.13′ E, Norderney Island, see Figure 1) on 8 September 2019 to acquire coastal wind profiles as part of the ongoing research project X-Wakes. In order to measure the wind at different height levels, a pulsed laser is used to infer, by means of aerosol reflection, the so-called radial wind speed, which can be calculated based on the frequency shift using the Doppler equation. An internal optical switch steers the laser beam at four azimuth angles in successive intervals of 90° (i.e. 0°, 90°, 180°, and 270°) to form a conical scan with a fixed elevation angle with respect to the horizontal. Those four radial wind speed vectors are combined by using the so-called Doppler-beam-swing (DBS) scan to determine the wind speed and wind direction (RAUSCH et al., 2022). The wind speed and direction, retrieved from the lidar system, are available at 25 height levels between 40 m and 500 m, with a vertical resolution of 10 m up to 100 m, 20 m up to 400 m, and 50 m up to 500 m. In the framework of this study, the wind speed and direction at 100 m altitude and for the time period from 1 April 2020 to 31 March 2021 are used for direct comparison of the wind speed with the closest grid point of the ERA5 and WRF model data, and therefore as a validation tool for the models' performance near the coast, as shown in Section 3.3. In order to ensure the data comparability between the different datasets, the filtering criteria described in CAÑADILLAS et al. (2011) is followed.

3.1.4 FINO1 mast

The offshore research platform FINO1 (LEIDING et al., 2016) is located in the German Bight in the North Sea (54° 0.864′ N, 7° 35.262′ E), approximately 45 km to the north of Borkum Island, at about 20 m above mean sea level (AMSL). The platform is equipped with a 101 m lattice tower, and has been operating since September 2003. The prevailing wind direction at FINO1 is south-west (CAÑADILLAS et al., 2020). The FINO1 data are available via the FINO database (BUNDESAMT FÜR SEESCHIFFFAHRT UND HYDROGRAPHIE (BSH), 2019). In the framework of this study, the wind speed from the top cup anemometer located at about 100 m is used for comparison with the closest grid points of the ERA5 and WRF models. Only the years 2005–2008 are used, since in these years the FINO1 mast measured the wind without the influence of a surrounding wind farm.

3.1.5 Airborne measurements

To investigate the coastal effects and spatial extent of wakes generated by offshore wind farms, several measurement flights were carried out within the X-Wakes project using the Dornier DO-128 research aircraft operated by the Technische Universität Braunschweig. The research aircraft is equipped with a nose boom to perform high-resolution measurements of the wind vector, temperature, humidity and pressure, sampling at a frequency of 100 Hz (CORSMEIER et al., 2001). Further, a sensor for measuring the surface temperature, a laser scanner for determining sea state characteristics and cameras were integrated (LAMPERT et al., 2020). The collected data enable the analysis of various atmospheric parameters like temperature profiles, as well as wind direction and wind speed over a larger area. Although the data are limited to a few hours and days, they provide an overview of the wind situation at different distances and heights both upstream and downstream of wind farm clusters and at different distances from the coast.

3.1.6 Satellite Synthetic Aperture Radar (SAR) data

Synthetic Aperture Radar (SAR) systems have become interesting instruments to assess surface wind speed at a resolution of a few hundred meters. The twin SAR

satellites from Copernicus Sentinel-1A and Sentinel-1B (TORRES et al., 2012; PETER et al., 2017) offer regular sampling of the German Bight around 5:00 UTC or 17:00 UTC with a repeated sampling pattern of 6 days. However, the same region can be sampled every one or two days depending on the incidence angle of the satellite. The SAR image mode used is Interferometric Wide (IW) swath mode with a size of 250 km and a resolution of 20 m. Satellite SAR acquires quantitative information about the state of the sea surface roughness through its backscatter intensity. Small-scale roughness enables access to oceanic and marine atmospheric boundary-layer processes (JOHANNESSEN et al., 1991; ALPERS and BRÜMMER, 1994). Near-surface wind speed is usually derived from calibrated normalized radar cross section (NRCS) using the geophysical model function (GMF) by knowing the wind direction and the incidence angle of the satellite. For Sentinel-1 acquisition at vertical polarisation (VV), the GMF is CMOD5N (PORTABELLA et al., 2002; HERSBACH et al., 2007; VERHOEF et al., 2008). For the 10-m wind speed retrieval, wind direction data are provided by the German Weather Service (DWD) (ZÄNGL et al., 2015). More details on the SAR wind speed retrieval can be found in DJATH et al. (2018); DJATH et al. (2022). The resolution of the retrieved wind field is about 400 m. Previous studies showed that the standard deviation between the SAR derived wind field and the in situ observation is about $1.9 \, \text{m s}^{-1}$ (HASAGER et al., 2011). As in DJATH et al. (2022), the analysis of the coastal effects concerns the relative quantities, therefore the resulting errors are almost negligible.

3.2 Methods

To describe our methodology, Section 3.2.1 explains how the hourly wind speed series were extracted from the ERA dataset, and Section 3.2.2 presents the estimation of atmospheric stability, Section 3.2.3 presents an empirical model of the horizontal wind speed gradient, and Section 3.3 describes the procedure for comparing ERA and WRF data with the observations at Norderney Island and the FINO1 offshore platform.

3.2.1 Extracting ERA5 wind speed

To investigate the horizontal wind speed gradients from the coast to open sea (139 km from the mainland), wind speed values are extracted at several ERA5 grid points, close to the location of the lidar on the island of Norderney (Figure 2) and towards the north at several altitudes. In addition to wind speed, other parameters are also extracted, namely air temperature (in K), specific humidity (in kg kg^{-1}), and sea surface temperature (SST) (in K), from which atmospheric stability can be derived (see Section 3.2.2). The wind speed (in m s^{-1}) is computed from the horizontal wind components u and v. For this analysis, the ERA5 data are not interpolated (neither spatially nor temporally). Two different ERA5 datasets
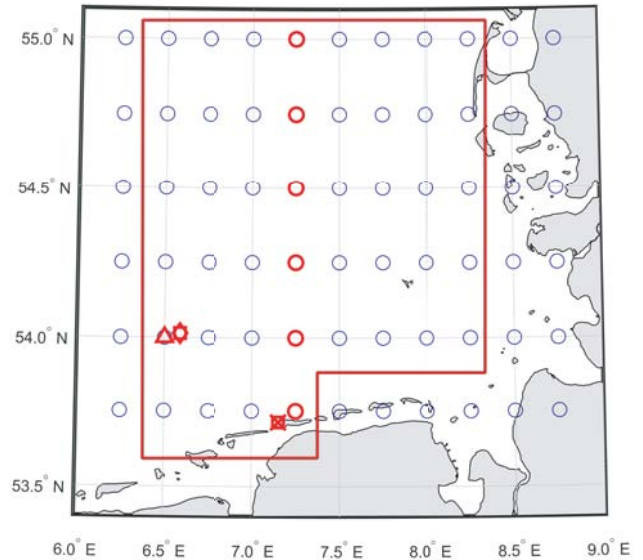

Figure 2: ERA5 grid points for the southern North Sea (blue dots), and selected for the analyses (red dots). The position of the wind lidar at the island of Norderney is indicated as a red cross. The position of FINO1 and the closest WRF grid points selected for the data comparison are marked with a red star and a red triangle respectively. The red polygon encompasses the grid points selected to estimate the variation of the wind speed gradient.

are used in this study. First, the ERA5 dataset for a single level contains surface level parameters (temperature at 2 m, surface pressure, mean sea level, etc.) and the horizontal wind components u and v at 10 m and 100 m altitude. The second dataset is based on pressure levels for different heights. For this study, the surface level at 10 m and the third highest pressure levels (namely, 1000 hPa ($\approx 110 \, \text{m} \pm 1.9 \, \text{m}$), 975 hPa ($\approx 320 \, \text{m} \pm 5.0 \, \text{m}$), 950 hPa ($\approx 540 \, \text{m} \pm 8.5 \, \text{m}$) are used to analyze the near surface from the ground to about 540 m altitude. Additionally, the wind speed at 875 hPa ($\approx 1300 \, \text{m} \pm 14.1 \, \text{m}$) is briefly used as a measure of wind speed without influence of surface roughness.

3.2.2 Atmospheric stability

We use the static atmospheric stability, which only takes into account buoyancy effects, and is characterized through the lapse rate (γ) based on the temperature gradient at two different altitudes, sea surface temperature (SST) and air temperature at 110 m corrected for air pressure, moisture and density effects to obtain the virtual potential temperature (θ_v) gradient,

$$\gamma = \frac{d\theta_v}{dz} \approx \frac{\Delta\theta_v}{\Delta z}, \tag{3.1}$$

with z the measurement height and the virtual potential temperature

$$\theta_v = T \left(\frac{p_0}{p}\right)^\kappa (1 + 0.61q), \tag{3.2}$$

Meteorol. Z. (Contrib. Atm. Sci.)
Early Access Article, 2023

B. Cañadillas et al.: Coastal horizontal wind speed gradients
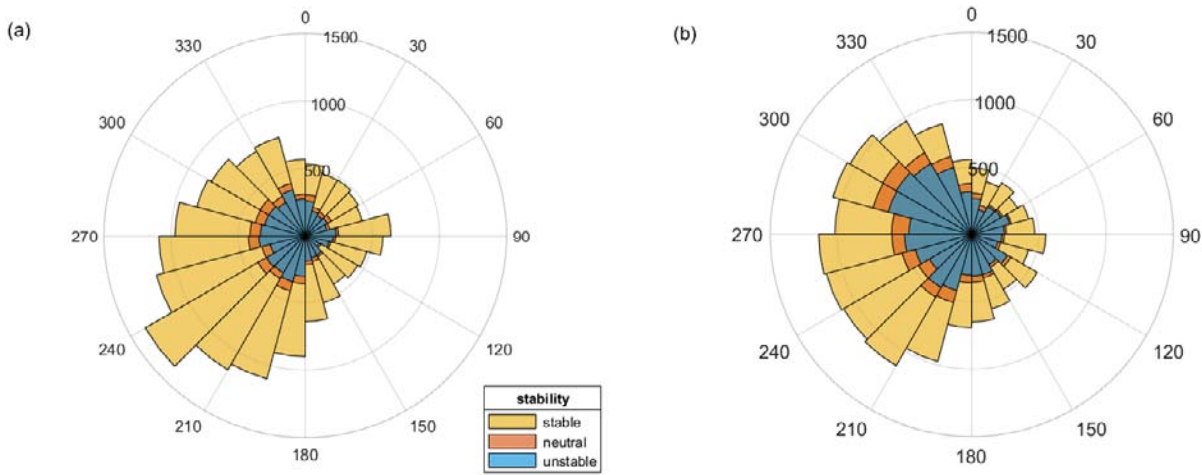
7

Figure 3: Directional distribution of atmospheric stability (lapse rate) for the layer between the surface and 110 m (1 January 2020–31 December 2021) for the (a) closest grid point to the lidar location and for the farthest (b).

with T the temperature (in K), p_0 and p the air pressure at mean sea level (both downloaded from ERA5 dataset) and at 110 m respectively, q the specific humidity and κ the ratio of the gas constant for dry air $R_{gas} = 287 \, \mathrm{J\,kg^{-1}\,K^{-1}}$ and the heat capacity of dry air $c_p = 1005 \, \mathrm{J\,kg^{-1}\,K^{-1}}$. Negative values of the virtual potential temperature gradient γ, or lapse-rate, represent an unstable stratification of the atmosphere, positive values represent a stable stratification, and values around zero represent a neutral stratification. As in PLATIS et al. (2022), the stability classes (in $\mathrm{K\,m^{-1}}$) are chosen as follows:

- $\gamma < -0.0005$: unstable stratification
- $-0.0005 \geq \gamma \leq 0.0005$: near-neutral stratification
- $\gamma > 0.0005$: stable stratification

Figure 3 shows stability roses for the ERA5 grid point closest to the coast and thus to the wind lidar (a) and the point farthest (139 km) from the coast (b) to illustrate the horizontal variability. The ERA5 grid point at the coast (Figure 3(a)) shows much more stable atmospheric conditions than in the grid further from the coast in the North Sea (Figure 3(b)). As expected, the further away from the coast, the more unstable the atmospheric conditions become, at least for the air layer analyzed (between the surface and 110 m).

3.2.3 Horizontal wind gradient model

The empirical one-dimensional model proposed by DJATH et al. (2022) helps quantify the relationship between relative wind speed R_u (defined in Eq. (5.1) at each ERA5 grid position (i)) and fetch x. The model considers three main parameters, namely, the wind speed at the coast, the equilibrium wind speed over sea (far offshore), and a characteristic adjustment length scale, and describes the increase in wind speed by the exponential function

$$R_u^f(x) = \alpha \left(1 - \exp\left(-\frac{x}{\sigma}\right)\right), \tag{3.3}$$

where α is defined as

$$\alpha = \left(\frac{u_{\mathrm{offshore}}}{u_{\mathrm{coast}}} - 1\right), \tag{3.4}$$

and σ describes the distance at which about 63 % of the final wind speed increase

$$\Delta u = u_{\mathrm{offshore}} - u_{\mathrm{coast}} \tag{3.5}$$

is observed. In addition, the equilibrium distance $x_{95\%}$ will be considered, at which the wind speed has increased to 95 % of its final value u_{offshore}. This distance can be expressed as

$$x_{95\%} = -\sigma \log\left(0.05 \frac{u_{\mathrm{offshore}}}{\Delta u}\right). \tag{3.6}$$

3.3 Comparison of ERA5/WRF with observational data

Prior to analyzing the horizontal wind gradients using the ERA5 reanalysis data, an inter-comparison of the hourly wind speed at 100 m height between the ERA5 reanalyses (and WRF model) and observations is performed for a period of one year (for the lidar measurement at the Norderney location) and three years (for the FINO1 mast located about 45 km off the German coast). Unfortunately, no overlapping data period is available at the Norderney and FINO1 locations, as the data period at the FINO1 mast is selected in a way to avoid any potential effect of the wind farm wake on the measurements. Therefore, care must be taken when comparing the wind conditions between the two locations due to inter-annual variation. The nearest ERA5 grid points to the observations (lidar/FINO1) as well as a two-dimensional linearly interpolated grid point (only at the lidar location) are selected for the inter-comparison (see Figure 2). To match the temporal resolution of ERA5/WRF, the lidar and FINO1 records (based on 10-min temporal resolution) were averaged to hourly data.

Table 2: Dataset, location and period used in the comparison.

Data	Location	Period
Lidar	53.7125° N, 7.152° E	
$ERA5_{\text{Norderney}}$	53.75° N, 7.25° E	01.04.2020–31.03.2021
$WRF_{\text{Norderney}}$	53.712° N, 7.152° E	
FINO1	54.014°N, 7.587°E	
$ERA5_{\text{FINO1}}$	53.75° N, 7.00° E	01.01.2005–31.12.2008
WRF_{FINO1}	54.014° N, 7.587° E	

Since mesoscale models are generally expected to be more accurate than reanalysis products in characterizing wind resources due to their finer spatial resolution and more comprehensive physics (PRONK et al., 2022), we compare also the observations with the WRF simulations (with a grid resolution of 2 km) to investigate whether a higher resolution model provides a better comparison with lidar, given the shortcomings of wind models in general at the coastal transition. Comparison with the FINO1 data allows us to check whether, as expected, the models (ERA5/WRF) compare better if the comparison location is far from the coastal line (as is the case of FINO1 mast location). Table 2 indicates the location of the observation and model grid points as well as the data periods used in this study.

It is worth mentioning that with this comparison we do not intend to carry out a deep validation of the models as this is not the purpose of this study but to get an idea of how the models perform at 100 m altitude, representative of the hub height for current wind turbines, and the only height investigated in the following section available at the two sites (coast and offshore within the area of the study). For a more in-depth validation of ERA5/WRF models, please refer to KALVERLA et al. (2019); HAHMANN et al. (2020); BRUNE et al. (2021).

We are aware that care must be taken when comparing model data to observations, as observations are commonly local to a particular point in space and time, rather than representing the averages of a model grid box.

Because of the topography of the southern part of the German Bight, the local wind coming from south is related to the coastal effects, which is the main focus of this study. Therefore, only southerly wind directions are selected for the following correlation analysis to avoid interference and other effects for wind from other directions. The analysis is based on the lidar dataset averaged over 1 h, and only the data with wind direction between 150°–210° are selected. The WRF dataset is hourly averaged and then synchronized with ERA5 (hourly resolution) according to the timestamp.

4 Case Studies using SAR, Flight, and Lidar Data for Land–Sea Flow

For flow from the land towards the sea, the transition from the atmospheric boundary layer to the marine atmospheric boundary layer (MABL) results in a flow readjustment to account for the reduced surface friction and often different surface temperature, and the establishment of an internal boundary layer (IBL) that grows with increasing fetch. Compared with the land surface roughness, the sea surface roughness can be two orders of magnitude lower, and over the North Sea during spring, the air–sea surface temperature difference (warmer air) can reach 10°–15 °C in the Northern Hemisphere spring (FOREMAN et al., 2015), leading to a very stable IBL for certain conditions. Typically, stable stratification offshore leads to a shallower IBL, which can extend to more than 50 km offshore (BARTHELMIE et al., 2007). Conversely, the IBL grows rapidly and merges into the MABL at a shorter distance in unstable conditions as the higher vertical mixing aids a more rapid flow adjustment. In either case, an increase of wind speed with increasing distance from the coast is frequently observed in the IBL due to the decrease of surface roughness. For example, according to an analysis performed by DJATH et al. (2022) using SAR data, the wind speed at 10 m height AMSL increases by a maximum of 45 % for fetch lengths of 100 km offshore.

Before presenting the results of the analysis of ERA5 data, we present case studies with SAR, flight and lidar observations to help reveal the mechanisms governing the land–sea horizontal wind speed gradients, especially considering whether the wind speed increases or decreases as observed in previous investigations (for example, KÄLLSTRAND et al., 2000; LAPWORTH, 2005; DJATH et al., 2022). We will see that the degree of the strong, onshore stratification is likely the governing influence determining whether the horizontal wind speed gradient is positive or negative with fetch. The quantification of the expected horizontal wind speed gradients is presented in Section 5.2 based on ERA5 data.

4.1 SAR and lidar observations

Here we show two cases of both increasing and decreasing wind speed gradients from the coast towards the sea, which have also been found in near-surface satellite derived wind fields (DJATH et al., 2022). Figure 4(a) displays a SAR image at 05:49 UTC on 31 August 2019 with the more common increase of wind speed with increasing fetch. An example of the wind speed that decreases with the distance from the coast, acquired at 17:16 UTC on 14 January 2020, is shown in Figure 4(b). For both cases, collocated 10-m wind field from ERA5 reanalysis are shown in Figure 4(c) and (d), respectively. The wind direction is from approximately south as seen by the wind barbs in panels (c) and (d), which also show wind speeds up to $10 \, \text{m s}^{-1}$ and $16 \, \text{m s}^{-1}$ in this region of the North Sea, respectively. The coastal wind gradients from SAR measurements are consistent with ERA5 reanalysis. In the first case Figure 4(a), the surface temperature over land to the south of the North Sea was about 16 °C, while at FINO1 it was approximately 19.5 °C. Hence, together with the reduced surface roughness offshore, there is a destabilization of the
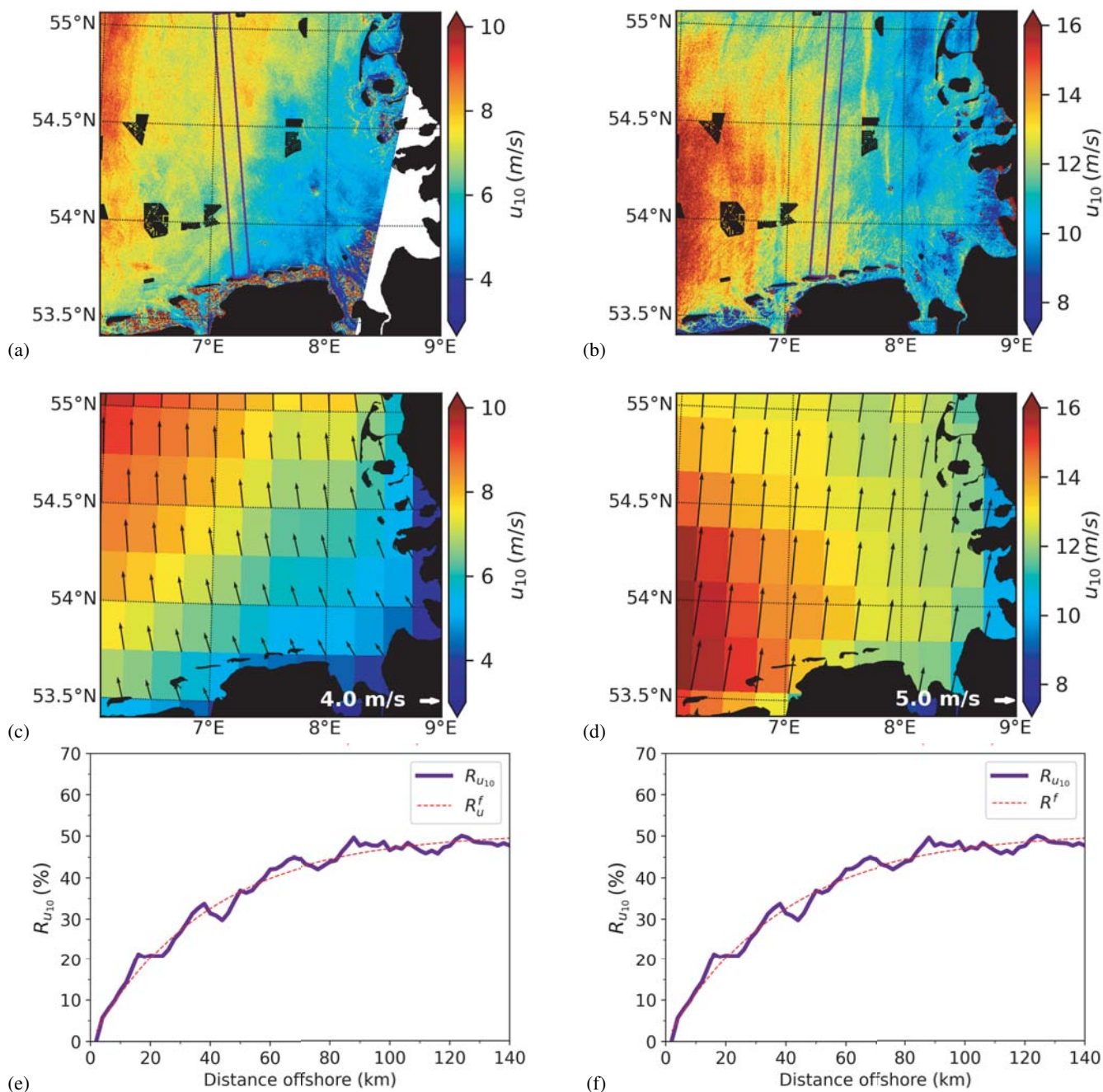
Meteorol. Z. (Contrib. Atm. Sci.)
Early Access Article, 2023

B. Cañadillas et al.: Coastal horizontal wind speed gradients

9

Figure 4: Derived 10-m wind speed from SAR image (a) and from ERA5 reanalysis (c) at 05:49 UTC on 31.08.2019. The FINO1 sea surface temperature was approximately 19.5 °C while it was about 16 °C over land at this time. Derived 10-m wind speed from SAR image (b) and from ERA5 reanalysis (d) at 17:16 UTC on 14.01.2020. The FINO1 sea surface temperature was approximately 7.7 °C while it was about 10 °C over land at this time. The relative wind speed ratio $R_{u_{10}}$ averaged over the blue region on 31.08.2019 (e) and 14.01.2020 (f). The red dotted line represents the empirical model fit from Eq. (3.3) for positive gradients and the dark blue solid line (R_u^f) the observations.

stratification, increased turbulence mixing and an acceleration of the 10-m wind speed as momentum is transferred downwards and there is less surface resistance. Figure 4(e) shows the corresponding relative increase of the 10-m wind speed averaged within the transect (blue box in Figure 4(a)) starting at the location of the lidar on Norderney Island and parallel to the wind direction. The wind speed increase reaches 45 % and the estimated adjustment distance is 77 km. As in DJATH et al. (2022),

the relative increase follows an exponential function (red dotted curve in Figure 4(e).

In the second case Figure 4(b), the surface temperature over land to the south of the North Sea was about 10 °C and probably stable given the time of year while the sea surface temperature at FINO1 was even cooler at 7 °C. Consequently, we have a stable flow over land that becomes even more stable as it flows over the sea which reduces the vertical mixing even further. For
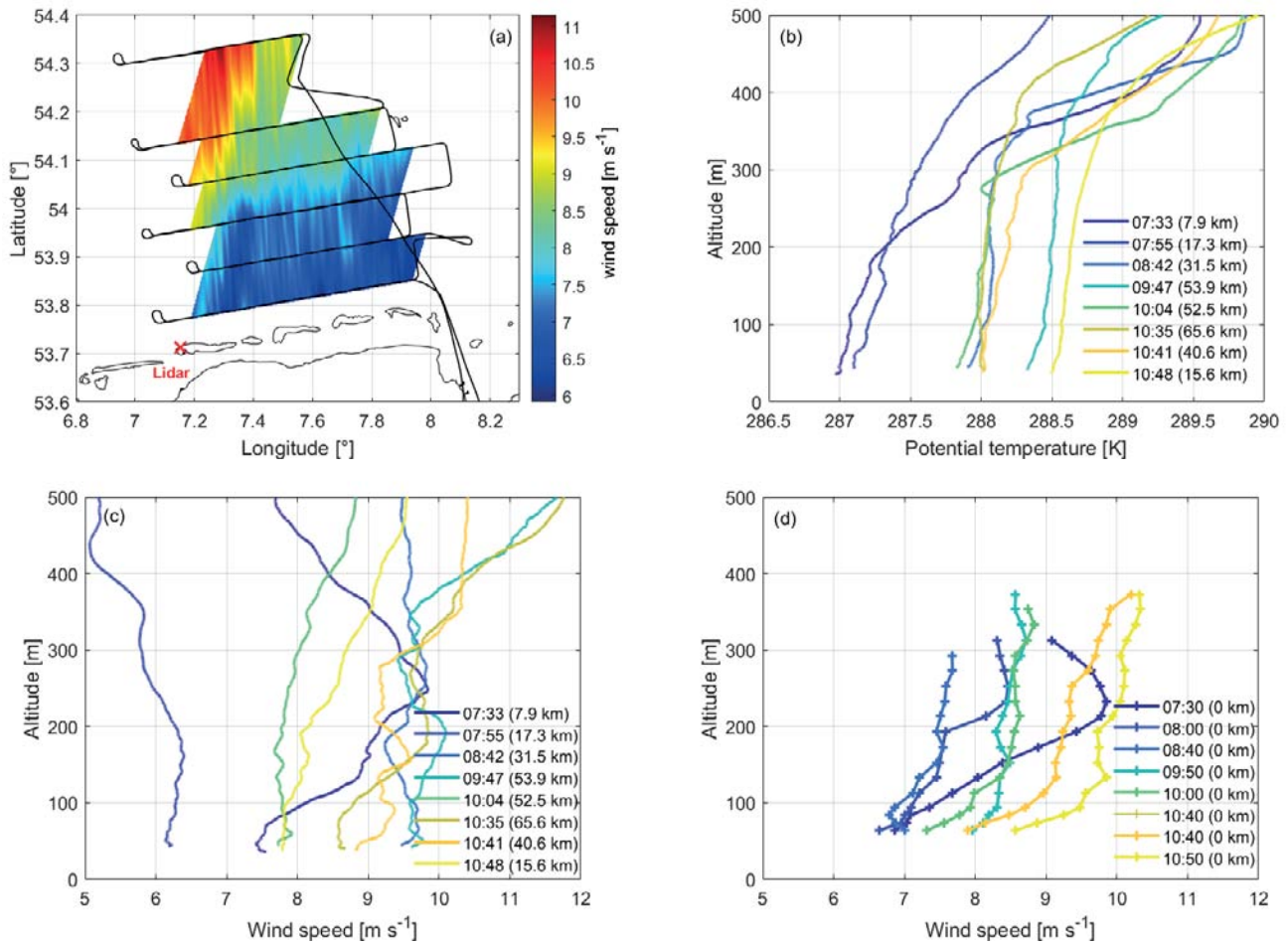
Figure 5: Aircraft and lidar observations from 7:05 to 11:03 UTC on 23 July 2020. The sea surface temperature at FINO1 was about 17 °C (290 K) while over land it was about 13 °C (286 K). (a) contour plot of interpolated aircraft wind field measurements along the mean wind direction at 100 m altitude, with the black line showing the flight trajectory. (b) Vertical profiles of potential temperature measured by the aircraft at various distances from the coast. (c) Vertical profiles of horizontal wind speed of the aircraft at various distances from the coast. (d) Corresponding (in time) vertical wind speed profiles measured by the lidar at the coast. The distance to the lidar and the measurement time are given in the legend for the vertical profiles. Note that in (b) and (c), the vertical profiles are first recorded with increasing and then decreasing distance from the coast.

such cases, temperature and wind speed profiles could help reveal some of the underlying mechanisms. Therefore, in the next case study, concurrent flight and lidar measurements with such vertical profiles are investigated.

4.2 Airborne and Lidar Observations

Aircraft observations from 23 July 2020 (from 7:05 UTC to 11:03 UTC) and 23 September 2020 (from 05:24 UTC to 08:53 UTC) are now used to examine two cases where the horizontal wind speed gradient increases and decreases, respectively, with distance from the coast. The research aircraft flew two similar flight patterns from the coast of Norderney on two separate days to capture the vertical and horizontal extent of the flow variation with increasing fetch. No SAR images are available for this case. The horizontal flight patterns (with the wind speed at 100 m indicated in colors) are shown in Figures 5(a) and 6(a) with flight legs perpendicular to the mean wind

direction (190° and and 215° respectively), and almost parallel to the southern coast. For both flights, linear interpolations were performed in the area between two adjacent legs to aid visualization of the development of the wind field. The boundary of the interpolated area was determined by the mean wind direction and the legs themselves. Figures 5(b) and 6(b) present vertical potential temperature profiles at various times and with increasing distance from the coast. These profiles are measured by making ascents at the conclusion of horizontal legs. The corresponding wind speed profiles during these ascents are presented in Figures 5(c) and 6(c). The lidar observed wind speed profiles at Norderney Island and at similar times to the vertical flight profiles are presented in Figures 5(d) and 6(d).

In the first case (Figure 5(a)), the surface temperature over land to the south of the North Sea was about 13 °C (286 K), while at FINO1 it was approximately 17 °C (290 K). The vertical potential temperature profile shown in Figure 5(b) closest to the coast (fetch
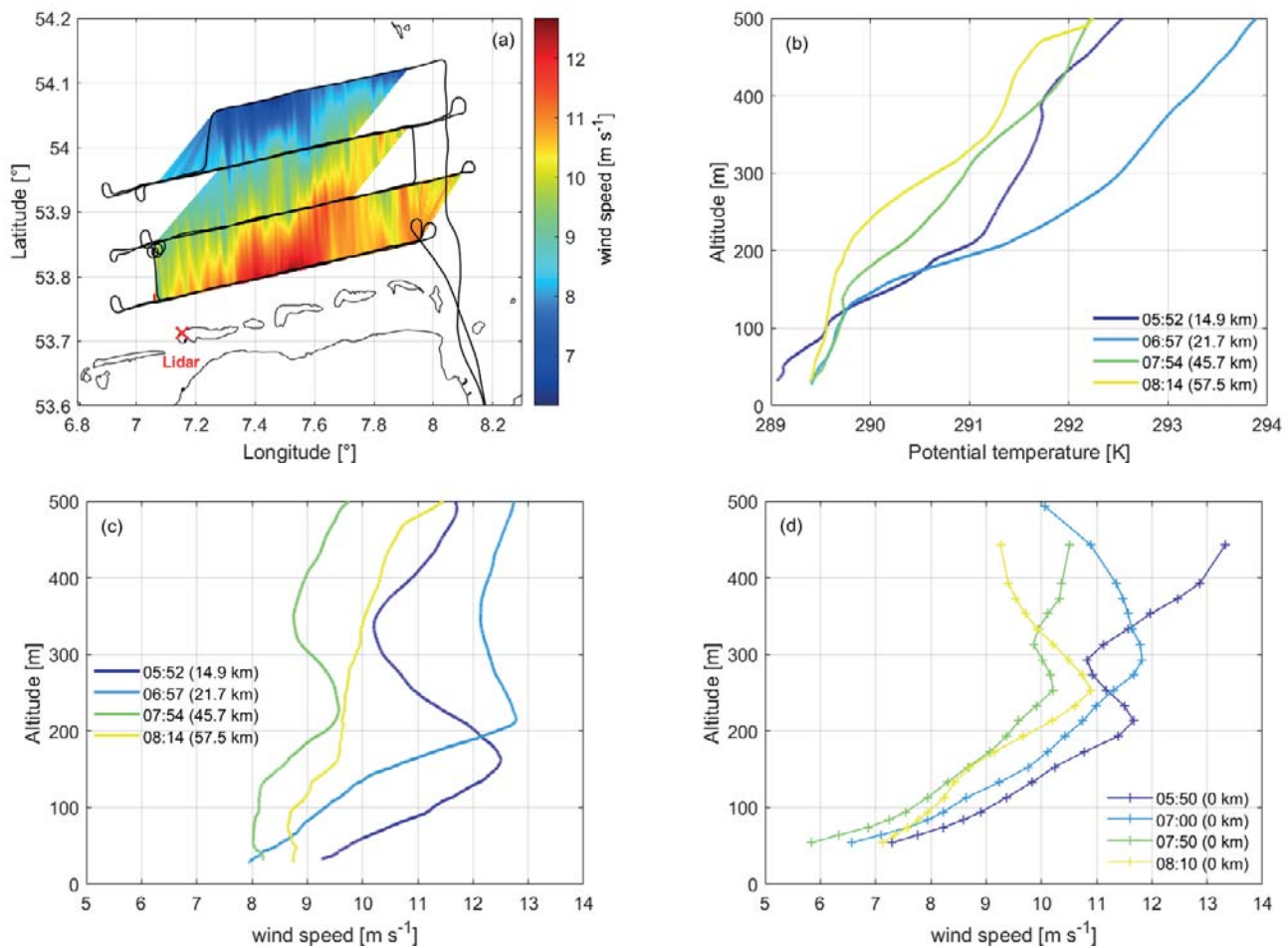
Meteorol. Z. (Contrib. Atm. Sci.)
Early Access Article, 2023

B. Cañadillas et al.: Coastal horizontal wind speed gradients

11

Figure 6: Aircraft and lidar observations from 05:24 to 08:53 UTC on 23 September 2020. The sea surface temperature at FINO1 was approximately 18 °C (291 K) while over land it was about 12 °C (285 K). (a) Contour plot of interpolated aircraft wind field measurements along the mean wind direction at 100 m altitude. The black line shows the flight trajectory. (b) Vertical profiles of potential temperature measured by the aircraft at various distances from the coast. (c) Vertical profiles of horizontal wind speed of the aircraft at various distances from the coast. (d) Corresponding (in time) vertical wind speed profiles measured by the lidar at the coast. The distance to the lidar and the measured time are given in the legend for the vertical profiles.

of 7.9 km) shows slightly stable conditions, and hence the corresponding LLJ over land is clearly visible in the wind speed profiles (dark blue) in Figures 5(c) and 5(d). Because of the higher sea surface temperature, the atmospheric stability is reduced with increasing fetch, vertical mixing is enhanced, enabling the vertical transfer of momentum down to lower levels, including the rapid disappearance of the LLJ already at 17.3 km from Norderney as seen in Figure 5(c). There is even an initial decrease in wind speed in this case as seen in the 7.9 km and 17.3 km profiles in Figure 5(c) and the 07:30 and 08:00 profiles of Figure 5(d). Later in the morning, surface heating over land would also reduce stability to unstable conditions, and hence the disappearance of the LLJ also at Norderney as seen at later times in Figure 5(d). Hence, the expected increase in wind speed over land following the classical variation of diurnal cycle (STULL, 1988) is also observed towards the middle of the day, which, for example at 100 m, increases from 7 m s^{-1} to 9.5 m s^{-1} in the time period shown at the lidar

position. This is in contrast with the offshore profiles which also show an increase in wind speed from 7 m s^{-1} to 9.5 m s^{-1} not just at 100 m above sea level, but also at 50 m above sea level, and thus more pronounced at lower levels, which is consistent with the ERA5 data shown below.

Consider now the alternate situation in Figure 6(a) illustrating a reduction in wind speed with increasing fetch. During this period, the surface temperature over land to the south of the North Sea was slightly lower at about 12 °C (285 K) compared with in the case above, with a sea surface temperature at FINO1 of 18 °C (291 K), and so also slightly warmer than during the case above. The key difference here is the strongly stable conditions over land as seen in the closest potential temperature profile to the coast recorded (blue) and shown in Figure 6(b). (Note that conditions onshore are probably even more stable than indicated because of the higher sea surface temperature at this particular profile position). In this case, a lapse rate over land of

up to $8\,\mathrm{K\,km^{-1}}$ is found in Figure 6(b) in contrast to the roughly $2\,\mathrm{K\,km^{-1}}$ indicated above in Figure 5(b). Because of the negative land–sea temperature gradient, the stable conditions are gradually weakened with increasing fetch as the lapse rate is reduced (Figure 6(b)) and the LLJ is gradually weakened and broken up (Figure 6(c)).

One can see that the flow and break-up of a LLJ for increasing fetch results in a complex, nonlinear height-dependent horizontal land–sea wind speed gradient. For example, Figure 6(b) shows that at $300\,\mathrm{m}$, there is first an increase in wind speed and then a decrease further out to sea while at $100\,\mathrm{m}$ there is a monotonic decrease. Such a complex behaviour is also evident in the ERA data in a minority of cases to be presented next.

5 Horizontal wind speed gradients derived from ERA5 reanalysis data

In Section 4 we have addressed some of the qualitative aspects of horizontal land–sea gradients using specific examples whereas in this section the quantification of these gradients is addressed, including their dependence on stability, using the much larger ERA5 database. Before deriving the horizontal wind speed gradients from the ERA5 reanalysis data, a comparison of these data with observational wind speed at Norderney Island and FINO1 is briefly presented to make a statement concerning the accuracy of the ERA5 data both near the coast (Norderney) and further from the coast (FINO1) (Section 5.1). The horizontal gradients themselves are then quantified in Section 5.2.

5.1 Observations Versus Models at FINO1 and Norderney Island

Appendix A gives the detailed results of the comparison of the ERA5 and WRF data with the wind speed measurements at Norderney Island and FINO1, both for wind directions only from the south ($150\,°–210\,°$) and for all wind directions. Despite the coarser resolution, the ERA5 data correlate better ($R^2 = 0.93$) than the WRF data ($R^2 = 0.85$) for the presented time period at Norderney Island (Figure A.1). Similar results are found with respect to the FINO1 mast for a longer period (($R^2 = 0.92$) for ERA5 and ($R^2 = 0.84$) for WRF), where there is noticeably more scatter (Figure A.2). Key performance indicators, including the bias, mean absolute error, root-mean-square error and squared Pearson's correlation coefficient are also presented in Appendix A. Based on these indicators, ERA5 is superior at the coast (Norderney), while the WRF model performs better (lowest bias, MAE and RMSE) at the offshore site (FINO1), however ERA5 still shows a better correlation. It is worth mentioning that no data assimilation has been used in the WRF simulations.

5.2 Horizontal Wind Speed Gradients Derived from ERA5 Reanalysis Data

Horizontal wind speed gradients from ERA5 (hourly data on pressure levels) relative to the ERA5 grid point closest to the coast are presented for a period of two years (1 January 2020 to 31 December 2021). We are aware that the use of a larger ERA5 dataset would likely result in more robust statistics, however, we do not expect a large deviation from results presented here, as these two years could be considered as representative of previous years when the current offshore wind turbines have been installed in the North Sea. Figure 2 shows the grid points used (red circles) perpendicular to the coast. We focus on flow from the south i.e., for flow from land towards the sea, with only wind directions within the sector ($150°–210°$) selected. The chosen sector width makes it possible to obtain a representative amount of data to produce robust statistics.

In order to quantify the horizontal wind speed gradients, we define a relative horizontal wind speed gradient as

$$R_{ui} = 100\left(\frac{\bar{u}_i}{\bar{u}_{\mathrm{coast}}} - 1\right), \qquad (5.1)$$

with $\bar{u}_{\mathrm{coast}}$ and $\bar{u}_i$ the mean hourly wind speed at the ERA5 grid point closest to the coast and the successive distances ($i = 28\,\mathrm{km}$, $56\,\mathrm{km}$, $83\,\mathrm{km}$, $111\,\mathrm{km}$ and $139\,\mathrm{km}$) from the coast, respectively. Equation (5.1) is first calculated for the whole dataset at four heights ($10\,\mathrm{m}$, $110\,\mathrm{m}$, $320\,\mathrm{m}$ and $540\,\mathrm{m}$) as shown in Figure 7(a), and then, similarly to DJATH et al. (2022), the relative mean wind speed gradients are divided into two groups: Figure 7(b) increasing wind speed, and Figure 7(c) decreasing wind speed, with distance from the coast by comparing the ERA5 grid points closest and furthest to the coast.

The proportion of data found in each of the three panels is presented in Table 3. Figure 7(a) reveals that the wind speed at all heights generally increases for flow from land to sea as the fetch increases. The wind speed gradient is more pronounced at lower heights and closer to the coast, before reaching an equilibrium between 60 and $80\,\mathrm{km}$ away from the coast. It is worth mentioning that the spatial variation of the relative wind speed including all ERA5 grid points within the area marked by a red polygon in Figure 2 is approximately $4\,\%$ at $110\,\mathrm{m}$ (not shown). At the model level heights of $10\,\mathrm{m}$ and $110\,\mathrm{m}$, the speed increases by up to $30\,\%$ and up to $20\,\%$, respectively, at a fetch of about $80\,\mathrm{km}$. At the measurement heights of $320\,\mathrm{m}$ and $540\,\mathrm{m}$, a relatively attenuated wind speed increase of up to $6\,\%$ is detected, probably due to the increased vertical separation from the influence of surface friction with respect to the heights of $10\,\mathrm{m}$ and $110\,\mathrm{m}$. The empirical model, fitted to the ERA5 data using a least-squares approach, (dashed lines in Figure 7(a)) indicates values of $32.4\,\%$ and $22.4\,\%$ with adjustment distance $x_{95\,\%}$ of about $49\,\mathrm{km}$ and $46\,\mathrm{km}$ (from Table 4) at $10\,\mathrm{m}$ and $110\,\mathrm{m}$ respectively.

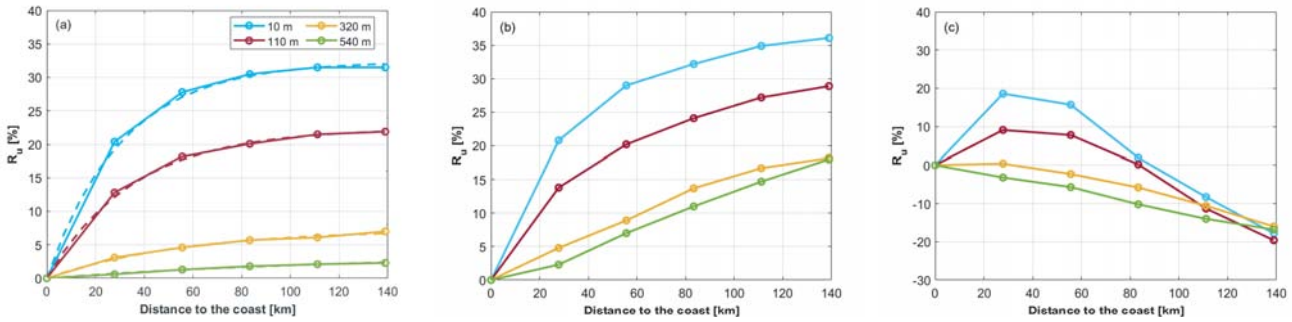**Figure 7:** Horizontal wind speed gradients relative to the grid point closest to the coast and for flow from the south (150–210°) and several heights (10 m, 110 m, 320 m and 540 m) above sea level. (a) All data, (b) only increasing wind speeds at each height, and (c) only decreasing wind speeds at each height. Dashed lines in (a) represent the empirical model fit from Eq. (3.3). The fraction of data comprising panels (b) and (c) for each height can be found in Table 3.

Table 3: Amount of ERA5 data (in percentage (absolute)) at all altitudes shown in Figure 7 for cases where the wind speed increases/decreases with distance from the coast.

	10 m	110 m	320 m	540 m
All data	3254	3162	2749	2400
increasing	89.9 % (2924)	85 % (2688)	73.8 % (2029)	67.2 % (1615)
decreasing	10.1 % (330)	15 % (474)	26.2 % (720)	32.8 % (785)

Figure 7(b) shows only the cases of increasing wind speed with increasing fetch, and these cases reveal an enhanced increase with respect to (a). At the larger heights of 320 m and 540 m, there is possibly a continuous linear increase of wind speed up to 138 km from the coast although we would expect this to eventually level off further offshore. Figure 7(c) shows cases where there is a decrease in wind speed, albeit with an initial increase within the first 60 km at the two lower heights, which is consistent with the wind profiles recorded during one of the flight campaigns (see Figure 6). There is a near-linear decrease of the wind speed with increasing fetch at the two larger heights in this case.

Figure 6 also reveals the presence of a LLJ at the coast which evolved into a standard wind speed profile further out to sea. To help summarize such a situation for all cases, Figure 8 displays the wind speed gradient based on the ERA5 110-m wind speed and the wind speed at 1300 m at the coastal grid point near Norderney against the difference in 2-m temperature measured at Norderney and FINO1 and the points are coloured depending on whether there is an increase (green) or decrease (red) in wind speed [%] from the coast to the location 139 km out to sea. We expect the 1300 m-wind speed to be relatively free from surface effects to approximate the geostrophic wind speed, so that if a LLJ is indeed present, then the ratio of the 110-m wind speed to the 1300 m wind speed will tend to be larger than unity. At the same time, if there is a transition from stable conditions over land to unstable over sea resulting in a reduction in wind speed, we would expect more points coloured red for negative $T_2 - \text{SST}$ values. Both of these are seen in Figure 8 where the negative gradi-
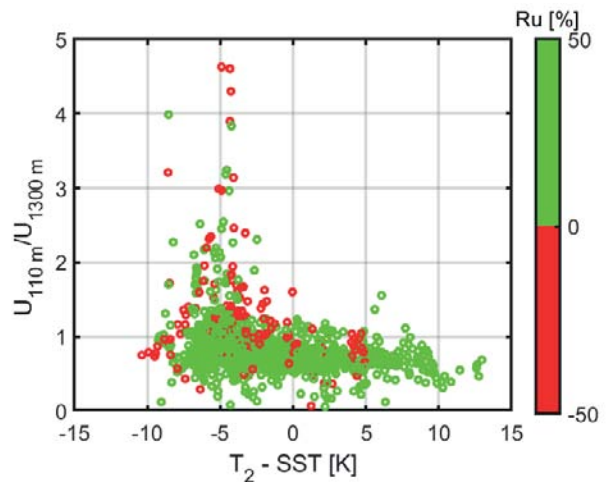

Figure 8: Ratio of the lidar 110-m wind speed versus the ERA5 1300-m wind speed as a function of the $T_2 - \text{SST}$ difference where T_2 is the 2-m air temperature at Norderney and the SST is recorded at FINO1. The colourbar indicates whether a positive (green) or negative (red) horizontal wind speed gradient R_u is detected.

ents (red) are generally higher than the positive gradients (green) and are found more toward the left where $T_2 - \text{SST} < 0°$ C.

Therefore, as suspected many years ago (e.g. PRYOR and BARTHELMIE, 1998), we confirm with the analyses that the wind speed at a potential offshore wind farm site is not solely dependent on fetch (distance from the coast) but also on the land–sea stability climate. To assess the impact of atmospheric stability on the horizontal wind speed gradient, we divide the ERA5 data into three at-
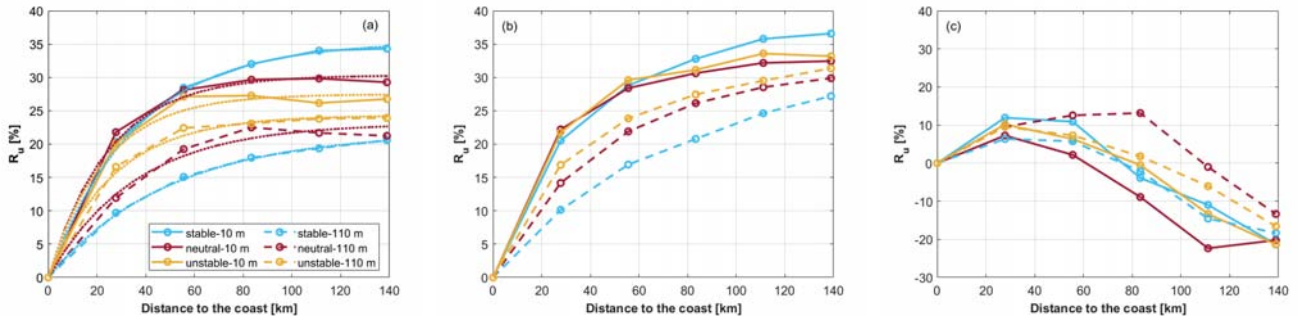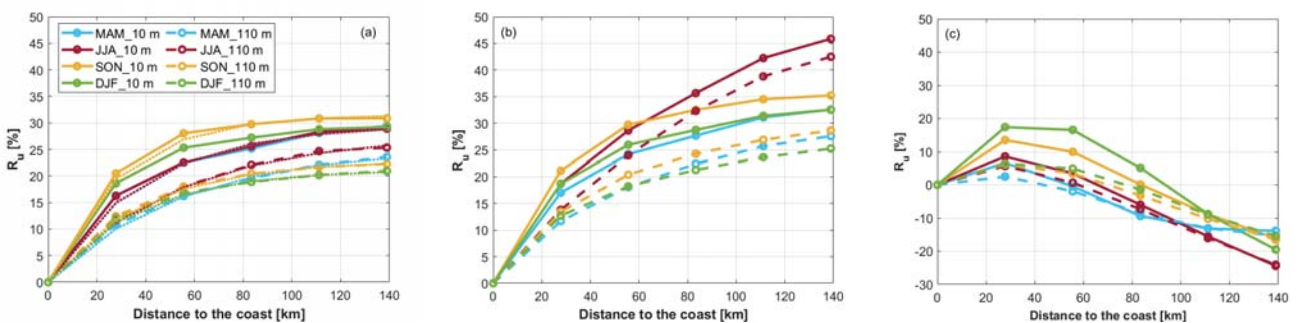
Figure 9: Relative horizontal wind speed gradient relative to the grid point closest to the coast for flow from the south (150°–210°) and grouped per atmospheric stability (unstable, neutral, and stable) at 10 m and 110 m above sea level. (a) All data, (b) only increasing wind speed at each height, and (c) only decreasing wind speed at each height. Dotted lines in (a) represents the empirical model fit from Eq. (3.3).

Figure 10: Relative horizontal wind speed gradient relative to the grid point closest to the coast and for flow from the south (150°–210°) and grouped per season (namely, spring (MAM, light blue line), summer (JJA, red lines), autumn (SON, yellow lines), and winter (DJF, green lines)) at 10 m, and 110 m above sea level. (a) All data, (b) only increasing wind speeds at each height (c), and only decreasing wind speeds at each height. Dotted lines in (a) represents the empirical model fit from Eq. (3.3).

mospheric stability groups, namely stable, neutral, and unstable conditions (Figure 9) according to the lapse rate estimated with Eq. (3.1) for the temperature profile at the coast. Figure 9(a) demonstrates that the wind speed gradients at 10 m and 110 m continue to increase in stable conditions some 138 km from the coast, but in neutral and unstable conditions the wind speed reaches equilibrium at about 80 km and 60 km, respectively. The ordering of the curves for the 110-m height is inverted to that at 10-m where the highest wind speed increase is found for stable, then neutral and unstable conditions, but at 110 m the ordering is unstable, neutral, and finally stable. This suggests that there is a net transfer of momentum to the 10-m level from the 110-m level in stable flow due to, for example, the disappearance of a LLJ for larger distances offshore (see Figure 5(c) above for an example of this). The stability wind roses (Figure 3) also show, in general, a transition to less stable conditions for increasing fetch x, which means less wind shear and a net transfer of momentum downwards.

A similar ordering is found in Figure 9(b) showing only increasing wind speed gradients, but for decreasing wind speed gradients in Figure 9(c) the picture is somewhat confused: the neutral and unstable curves group

somewhere together, with the stable curve at 110 m sitting above, and the 10-m stable curve below. This is somewhat similar to the case above in Figure 6(c) where there is a general deceleration of the flow in very stable conditions, more delayed with fetch at higher levels, but stronger at lower levels. The case-to-case details though will likely vary depending on the exact nature of the wind profile or LLJ. Further clues can possibly gleaned from the probability density plots of the wind speed gradients presented in Figure C.1. In general, the 10-m distributions are skewed right to positive gradients, with the distributions tending towards more symmetric Gaussian shapes with increasing height.

Seasonal differences may be a superior classification to the coastal static stability. Figure 10 presents the relative horizontal wind speed gradients grouped according to the seasons (namely, winter (December–January–February, DJF), spring (March–April–May, MAM), summer (June–July–August, JJA) and autumn (September–October–November, SON)) for the heights of 10 m (the standard height used to infer wind speed from SAR data) and 110 m (representative hub height for current wind turbines). Wind speed increases are generally observed at both heights (Figure 10(a)), being stronger

Meteorol. Z. (Contrib. Atm. Sci.)
Early Access Article, 2023

B. Cañadillas et al.: Coastal horizontal wind speed gradients

15

Table 4: Recapitulation of parameters obtained for fitting processes in Figures 7, 9 and 10 using Equation (3.3), where $R_{u\,138\,km}$ is the maximum increase in the relative wind speed and $x_{95\,\%}$ is the distance at which the wind speed reaches 95 % of its equilibrium value.

Mean	10 m	110 m	320 m	540 m
$R_{u\,138\,km}$ [%]	32.4	22.4	7.3	3.5
$x_{95\,\%}$ [km]	49	46	17	–
Seasons	**MAM** (10 m/110 m)	**JJA** (10 m/110 m)	**SON** (10 m/110 m)	**DJF** (10 m/110 m)
$R_{u\,138\,km}$ [%]	29.7 / 29.7	27.9 / 26.8	31.6 / 22.9	29.6 / 21.2
$x_{95\,\%}$ [km]	62 / 76	61 / 78	45 / 48	49 / 50
Stability	**stable** (10 m/110 m)	**neutral** (10 m/110 m)	**unstable** (10 m/110 m)	
$R_{u\,138\,km}$ [%]	35.3 / 21.8	30.3 / 23.1	27.5 / 24.3	
$x_{95\,\%}$ [km]	59 / 62	38 / 47	33 / 36	

in autumn and winter, and slightly weaker in spring and summer at the height of 10 m AMSL, although the ordering is not as clear as in Figure 9(a).

Here, at 110 m, gradients are slightly more consistent between the different seasons. Figure 10(b) presents cases with only increasing wind speeds, showing that the highest increase occurs in spring and summer, and at both the 10 m and 110 m levels 138 km from the coast. Such cases are likely dominated by positive land–sea temperature differences and hence a transition from unstable to stable flow in which the reduced roughness and turbulence results in the expected speed-up offshore. At the same time, Figure 10(c), considering only negative wind speed gradients, also reveals the highest reduction in autumn and summer and it is in these cases when a LLJ occurs over land after strong night-time surface cooling, resulting in a flow from stable to unstable conditions as presented in the case in Figure 6.

Table 4 quantifies the average strength and extent of the horizontal wind speed gradients. The wind speed increases by roughly 30 % at 10 m, reducing to about 3 % at a height of 540 m AMSL. Of interest for wind energy purposes, the 110-m wind speed increases by slightly more than 20 % within the first 46 km from the coast. This may increase to approximately 60 km during stable conditions and even about 75 km in spring and summer; the increase remains, however, at about 25 % of the coastal wind speed.

6 Discussion and conclusions

Understanding coastal effects is a complex task that requires spatial information in both directions, horizontal and vertical. To be able to capture all relevant temporal and spatial scales a combination of observation and model is required. This study aimed to describe coastal wind gradients for flow from land to sea.

Before analysing the horizontal wind speed gradients by using ERA5 reanalysis data, a vertical wind lidar located on Norderney Island near the German mainland acts as our observational reference for the ERA5 data,

where a good agreement ($R^2 = 0.93$) is found despite the relatively coarse ERA5 data resolution. Interestingly, the comparison of lidar data with the higher-resolution Weather Research and Forecasting (WRF) mesoscale model yields a good but relatively weaker agreement ($R^2 = 0.85$). Contrary to expectations, it appears that ERA5 performs better at the coast than the WRF model. As the WRF model used the ERA5 data as initial boundary conditions, it appears that the downscaling methods used in the WRF have to be adjusted in the transition to the coast. The origin of these differences could be traced back to the mixing length in the turbulence closure scheme used in the mesoscale model, as pointed out in SKYLLINGSTAD et al. (2005). However, the parameterization of sea roughness, changing land-use due to tides or SST input values, which seems to be overestimated when compared with the aircraft measurement (not shown), could also have a major influence. At the offshore location investigated in this study (FINO1), the WRF model performs better (lower bias, MAE and RMSE) than ERA5, although ERA5 still has a higher correlation coefficient ($R^2 = 0.92$ versus $R^2 = 0.84$).

The examination of the horizontal wind speed gradients extending north from the southern coast of the German Bight indicate a general trend of increasing wind speed with increasing fetch, dependent strongly on the height above the sea surface, and weakly on the season and atmospheric stability. The less common (10 %) decrease in wind speed with increasing fetch is generally associated with stable conditions over land, which can result in the formation of a LLJ at the coast, which, when encountering the warmer SST, is broken up under the influence of enhanced vertical mixing and turbulence found in unstable conditions, resulting in a flow deceleration and the formation of the classic logarithmic wind speed profile offshore. Nonetheless, based on the exponential model fitted to the ERA5-derived horizontal wind speed gradients, we are able to make some general quantitative statements about the strength of the more common positive wind speed gradients. Within the first 110 m altitude AMSL, the wind speed will generally reach its equilibrium wind speed within ap-

Table A.1: KPI values for wind speed at 100 m height for all and for only flow from the south between the lidar (Norderney) and cup anemometer (FINO1) observations and ERA5 and WRF results (values in bracket).

	N°data	KPI − ERA5 (WRF)			
		$BIAS m\,s^{-1}$	$MAE m\,s^{-1}$	$RMSE m\,s^{-1}$	R^2
Lidar (Norderney) all wind directions	7870	0.11 (−0.39)	0.12 (0.39)	0.13 (0.41)	0.91 (0.81)
Lidar (Norderney) only south wind directions	1835	0.06 (−0.56)	0.093 (0.57)	0.11 (0.67)	0.93 (0.85)
FINO1 all wind directions	34353	0.35 (0.12)	0.35 (0.12)	0.3 (0.15)	0.92 (0.83)
FINO1 only south wind directions	6195	0.28 (0.21)	0.28 (0.22)	0.31 (0.24)	0.92 (0.84)

proximately 50 km of the coast, having increased some 20–30 % above the coastal wind speed. Stable conditions tend to increase the distance that the equilibrium wind speed is reached by approximately 10 km while neutral/unstable conditions will reduce it by approximately 10 km. The practical consequences here are that large wind farms within 50 km of the coast and oriented in something other than a parallel arrangement with the coast may be affected by significantly different wind resources within the wind farm, assuming that there is a significant land–sea flow component, such as e.g. found in UK or Denmark in Northern Europe as a couple of examples. Moreover, such phenomena become more frequent if there is a significant number of stably stratified flow periods of warm air flowing over cooler water. The empirical results and model proposed may aid planners and operators in accounting for such inhomogeneous within-farm flow phenomena in their resource assessment tools.

Acknowledgments

A   Comparison of ERA5/WRF with observational data for all wind directions

Figures A.1 and A.2 show density scatter plots and linear regressions between ERA5 and WRF datasets versus observations (lidar at Norderney and FINO1 mast cup anemometer), respectively, for flow from the south (from land). Moreover, the ERA slope and y-intercept are closer to one and zero, respectively. To assess the ability of the ERA5 reanalysis and WRF model to capture the hourly wind speed observations (lidar/FINO1) at 100 m, we compute four key performance indicators (KPIs), namely the bias which represents the mean error (*Bias*), the mean absolute error (*MAE*), the root-mean-square error *RMSE*, which represents the standard deviation of the residual (where the residual is a measure of how far away the values are from the regression line) and the square of Pearson's correlation coefficient (R^2), which represents the degree of dispersion between observations and models (precision), as follows:

$$Bias = \frac{1}{n}\sum_{i=1}^{n} o_i - m_i, \tag{A.1}$$

$$MAE = \frac{1}{n}\sum_{i=1}^{n} |o_i - m_i|, \tag{A.2}$$

$$RMSE = \sqrt{\frac{1}{n}\sum_{t=1}^{n}(o_i - m_i)^2}, \tag{A.3}$$

$$R^2 = \frac{\sum_{t=1}^{n}(m_i - \bar{o})^2}{\sum_{t=1}^{n}(o_i - \bar{o})^2}. \tag{A.4}$$

Here, o_i and $\bar{o}$ are the values of the i_{th} and mean of the observations (lidar/FINO1), and m_i the i_{th} value of the model (ERA5/WRF) at time i for a time series of length n. The results of this analysis are summarized in Table A.1 both for only southerly winds and for all wind directions. Based only on R^2, the ERA5 data are better correlated with both the observations at Norderney and

Meteorol. Z. (Contrib. Atm. Sci.)
Early Access Article, 2023

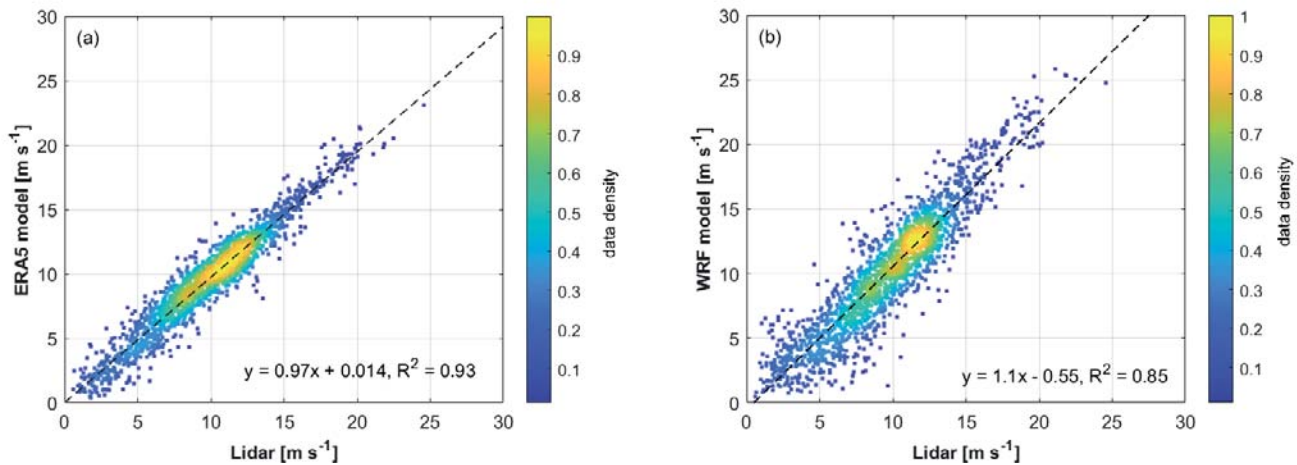B. Cañadillas et al.: Coastal horizontal wind speed gradients

17

Figure A.1: Hourly wind speed density correlation for only flow from the south (150°–210°) between the lidar and ERA5 (a) and lidar and WRF (b) datasets for the period 01.04.2020 to 31.03.2021 at a 100-m height at Norderney Island.
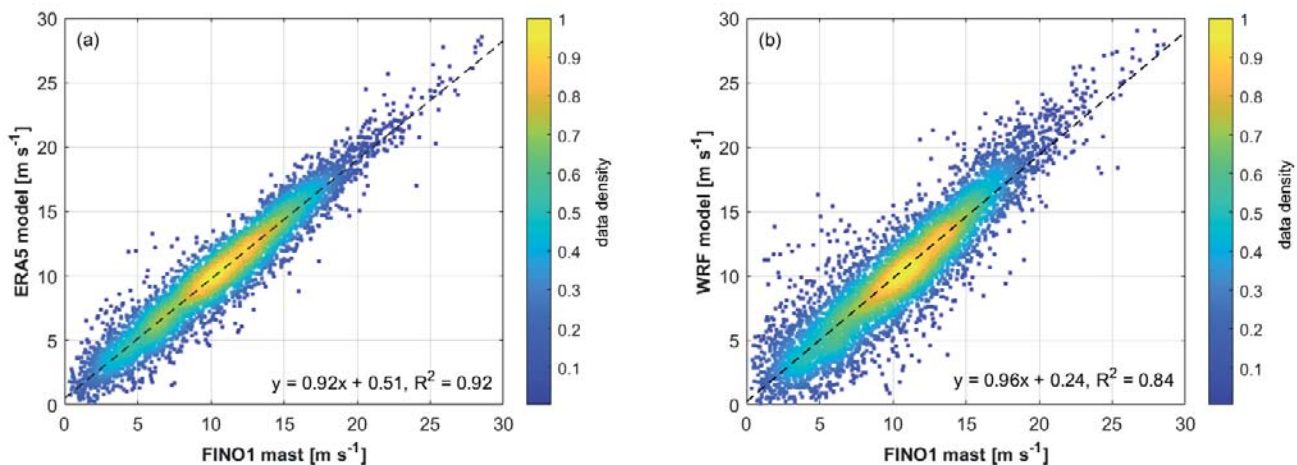

Figure A.2: Hourly wind speed density correlation for only flow from the south (150°–210°) between the FINO1 cup anemometer and ERA5 (a), and FINO1 cup anemometer and WRF (b) datasets for the period 01.01.2005 to 31.12.2008 at the 100 m height.

FINO1 compared with the WRF model. Based on the other indicators (*Bias*, *MAE*, *RMSE*), the WRF model performs better at FINO1, but not at Norderney.

Figure A.3 shows monthly averaged time series (a) and the average diurnal cycle (b) at Norderney for all models and observations and for the flow from the south only. Similarly, Figure A.4 shows the monthly-averaged annual cycle (a) and hourly-averaged diurnal cycle (b) at FINO1 for only flow from the south. Overlaid in the figures are the number of data points used. The same data period is used for these figures as for the correlations. The monthly time series shows a clear seasonal variation with lower wind speeds in summer and higher wind speeds in autumn–winter.

A diurnal cycle is only weakly evident in all wind directions (not shown), but is clearly evident in the southern wind directions, with the maximum offshore wind speed occurring in the early evening. This once more points to the temperature contrast over land with the sea

surface having a key role in the development of the offshore flow.

At the coast (lidar location), the ERA5 reanalysis seems to have a better match with the observations, showing a slight underestimation in the monthly wind speed, while the WRF model seems to overestimate the wind speed for most months. At the offshore location, both monthly-averaged datasets are very well correlated with the FINO1 data. The diurnal cycles shown in Figure A.3 at the coast and Figure A.4 offshore reveal a maximum wind speed in the period 17:00–21:00 UTC and not at noon as expected over land. This delay is consistent with that found in LAPWORTH (2005) that the maximum offshore wind speed is generally found during the cooled evening land (negative land–sea temperature gradients) and unstable offshore flow – the minimum offshore wind speed is found during the middle of the day (most stable flow). A similar effect is observed at FINO1, however the effect seems to be weaker
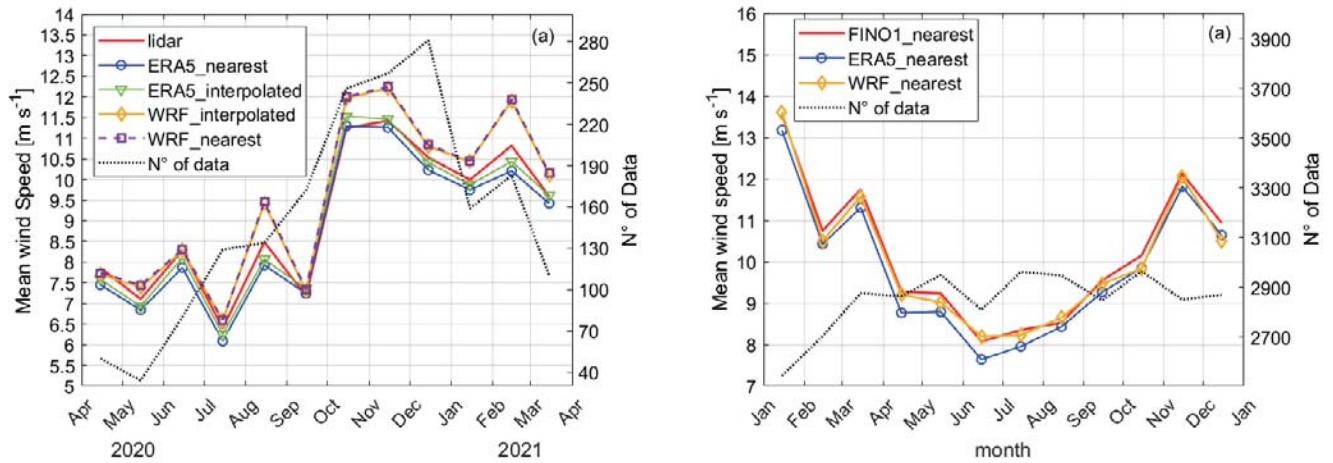
Figure A.3: Monthly averaged time series (a) and the hourly averaged diurnal cycle (b) of the wind speed according to lidar observations (Norderney, coast) and the ERA5/WRF results at 100 m AMSL for flow from the south (150°–210°). The closest interpolated grid points are displayed to show the sensitivity to the method.
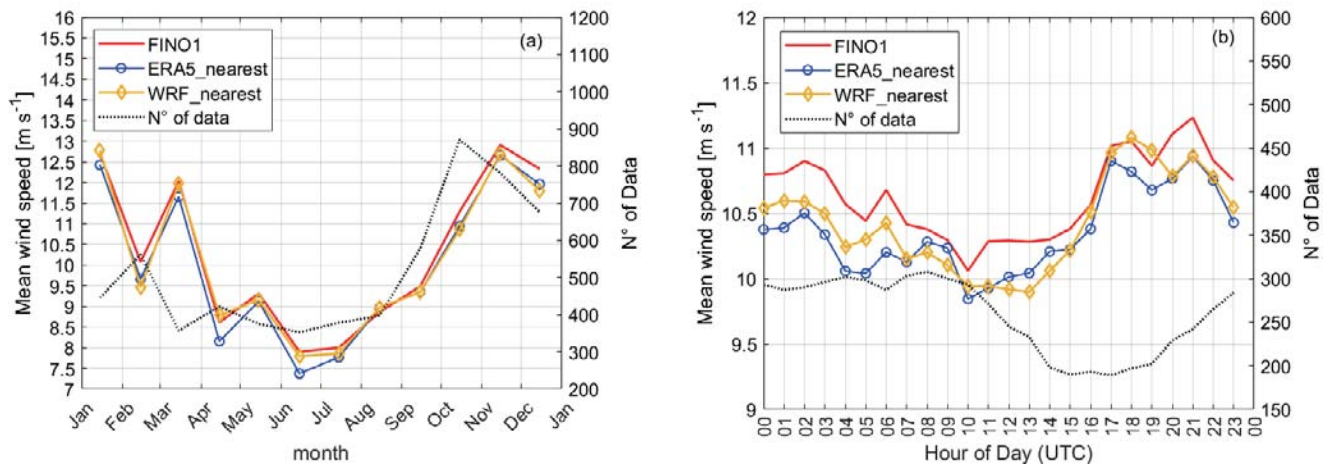
Figure A.4: Monthly averaged annual (a) and hourly averaged diurnal (b) cycles of the wind speed of FINO1 observations (offshore) and ERA5/WRF results at 100 m for flow from the south (150°–210°).

and happens slightly later than at the coast. Consistent with the onshore and offshore comparison of PRONK et al. (2022), the coastal ERA and WRF data slightly underestimate and overestimate the diurnal cycle of wind speed, respectively, while offshore, both the ERA and WRF data slightly underestimate the wind speeds. Both datasets show similar seasonal and diurnal patterns, with the WRF model tending to overpredict the amplitude of the diurnal wind speed cycle at the coast during most of the daytime hours, except during 11:00–13:00 UTC. At the offshore site (FINO1), both models underestimate the diurnal cycle, with WRF being a better fit to the observations.

From the comparisons shown above at the lidar position (at the coast) it appears that, contrary to expectations, the WRF simulations show a larger discrepancy with the lidar than the ERA5 which have a much larger spatial resolution than WRF (31 km versus 2 km for WRF). The question here is whether this discrepancy

is due to the complexity of the offshore wind due to, for example, the abrupt change of the roughness or due to the downscaling method. Note that WRF uses ERA5 as the initial boundary conditions. Mesoscale models are known to have higher uncertainties offshore if winds come from land (HAHMANN et al., 2015).

B ERA5 wind conditions with distance to shore

Figure B.1 provides a general picture of the wind conditions at 100-m height from the study target area by considering 2 years (2020–2021) of ERA5 data. In Figure B.1(a) the wind rose for the period 2020–2021 at all ERA5 grid positions and at 100 m AMSL is presented. The wind rose indicates a clear predominance of northwesterly, westerly and southwesterly winds with increasing southwesterly winds as we approach the
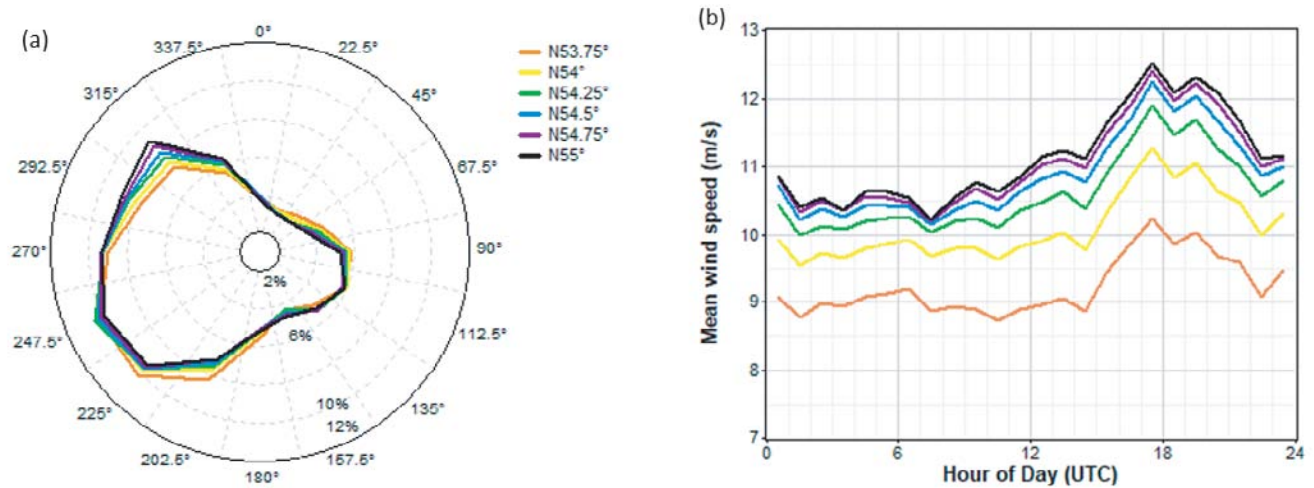
Figure B.1: ERA5 statistics for the period 2020–2021 at 100 m with increasing distance from the coast (at each ERA5 grid point selected): (a) wind rose, and (b) diurnal cycle for only south directions.
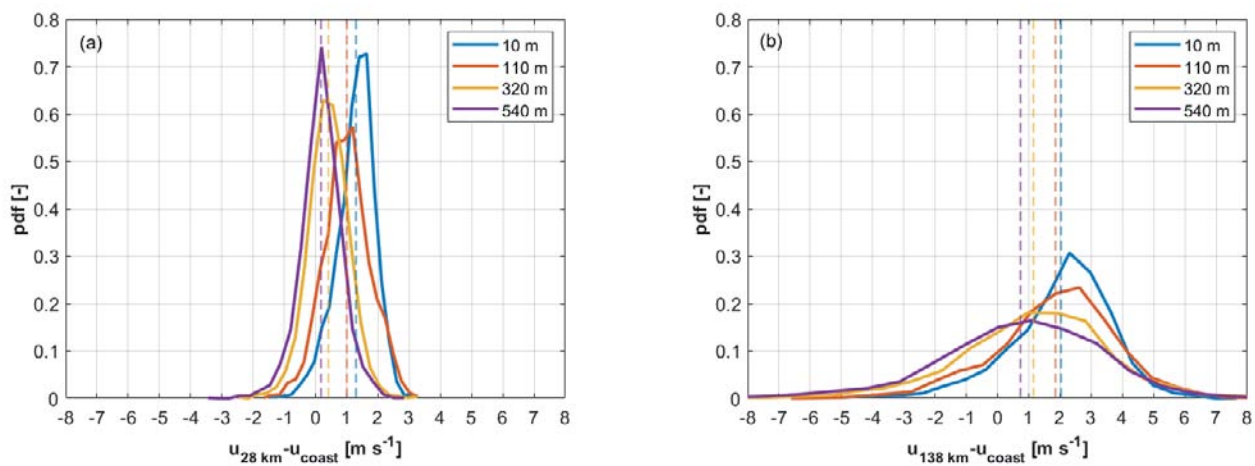

Figure C.1: ERA5 probability density distribution (pdf) wind speed bias ($u_i - u_{\text{coast}}$) between the coast and (a) 28 km and (b) 138 km for all heights analysed and for only southerly winds. Mean value is indicated by vertical dashed lines.

coast. According to EMEIS et al. (2016) and based on FINO1 data southwesterly winds are associated with stable conditions. The diurnal cycle (Figure B.1(b)) for southerly winds only (150°–210°) shows a maximum around 18:00 UTC with wind speed increasing with distance from the coast.

C ERA5 probability density functions for only southerly winds

Figure C.1 shows the probability density functions of the wind speed gradient ($u_i - u_{\text{coast}}$) for two different distances to the coast ($i = 28$ km, and 139 km) and at the four heights investigated (10 m, 110 m, 320 m and 540 m) and for southerly winds only. This display reveals how the values are distributed around the means presented in Figure 7. For all heights, the hourly bias is mostly positive, indicating that the wind speed is higher offshore, as expected. The skewness of the distributions

decreases with height, with a nearly symmetric distribution with a mean of about 0.72 m s^{-1} per 138 km at 540 m height. This may indicate that synoptic weather phenomena are prevalent at these heights. However, further work is needed to better understand the interaction of coastal effects with synoptic weather phenomena, such as the passage of cold fronts as outlined in SCHULZ-STELLENFLETH et al. (2022).

References

AHSBAHS, T., M. BADGER, P. VOLKER, K.S. HANSEN, C.B. HASAGER, 2018: Applications of satellite winds for the offshore wind farm site anholt. – Wind Energy Sci. **3**, 573–588, DOI: 10.5194/wes-3-573-2018.

AHSBAHS, T., G. MACLAURIN, C. DRAXL, C.R. JACKSON, F. MONALDO, M. BADGER, 2020: US East Coast synthetic aperture radar wind atlas for offshore wind energy. – Wind Energy Sci. **5**, 1191–1210, DOI: 10.5194/wes-5-1191-2020.

ALPERS, W., B. BRÜMMER, 1994: Atmospheric boundary layer rolls observed by the synthetic aperture radar aboard the ERS-1 satellite. – J.Geophys. Res. **99**, 12613–12621.

ARCHER, C., S. WU, Y. MA, P. JIMENEZ, 2020: Two corrections for turbulent kinetic energy generated by wind farms in the wrf model. – Mon. Wea. Rev. **36**, 285–299, DOI: 10.1175/MWR-D-20-0097.

BARTHELMIE, R., M. COURTNEY, J. HØJSTRUP, S.E. LARSEN, 1996a: Meteorological aspects of offshore wind energy: Observations from the vindeby wind farm. – J. Wind Engineer. Indust. Aerodyn. **62**, 191–211, DOI: 10.1016/S0167-6105(96)00077-3.

BARTHELMIE, R., J. BADGER, S. PRYOR, C. HASAGER, M. CHRISTIANSEN, B. JØRGENSEN, 2007: Offshore coastal wind speed gradients: Issues for the design and development of large offshore windfarms. – Wind Engineer. **31**, 369–382, DOI: 10.1260/030952407784079762.

BARTHELMIE, R.J., 1999: The effects of atmospheric stability on coastal wind climates. – Meteor. Appl. **6**, 39–47, DOI: 10.1017/S1350482799000961.

BARTHELMIE, R.J., 2001: Evaluating the impact of wind induced roughness change and tidal range on extrapolation of offshore vertical wind speed profiles. – Wind Energy **4**, 99–105, DOI: 10.1002/we.45.

BARTHELMIE, R.J., B. GRISOGONO, S.C. PRYOR, 1996b: Observations and simulations of diurnal cycles of near-surface wind speeds over land and sea. – J. Geophys. Res. Atmos. **101**, 21327–21337, DOI: 10.1029/96JD01520.

BRUNE, S., J.D. KELLER, S. WAHL, 2021: Evaluation of wind speed estimates in reanalyses for wind energy applications. – Advan. Sci. Res. **18**, 115–126, DOI: 10.5194/asr-18-115-2021.

BUNDESAMT FÜR SEESCHIFFFAHRT UND HYDROGRAPHIE (BSH), 2019: Fino datenbank. – https://www.fino1.de/de/ Last accessed: 30.06.2022.

CAÑADILLAS, B., A. WESTERHELLWEG, T. NEUMANN, 2011: Testing the performance of a ground-based wind lidar system: One year intercomparison at the offshore platform fino1. – DEWI Mag. **38**, 58–64.

CAÑADILLAS, B., R. FOREMAN, V. BARTH, S. SIEDERSLEBEN, A. LAMPERT, A. PLATIS, B. DJATH, J. SCHULZ-STELLENFLETH, J. BANGE, S. EMEIS, T. NEUMANN, 2020: Offshore wind farm wake recovery: Airborne measurements and its representation in engineering models. – Wind Energy **23**, 1249–1265, DOI: 10.1002/we.2484.

CORSMEIER, U., R. HANKERS, A. WIESER, 2001: Airborne turbulence measurements in the lower troposphere onboard the research aircraft dornier 128-6, d-ibuf. – Meteorol. Z. **10**, 315–329, DOI: 10.1127/0941-2948/2001/0010-0315.

DEE, D.P., S.M. UPPALA, A.J. SIMMONS, P. BERRISFORD, P. POLI, S. KOBAYASHI, U. ANDRAE, M.A. BALMASEDA, G. BALSAMO, P. BAUER, P. BECHTOLD, A.C.M. BELJAARS, L. VAN DE BERG, J. BIDLOT, N. BORMANN, C. DELSOL, R. DRAGANI, M. FUENTES, A.J. GEER, L. HAIMBERGER, S.B. HEALY, H. HERSBACH, E.V. HÓLM, L. ISAKSEN, P. KÅLLBERG, M. KÖHLER, M. MATRICARDI, A.P. MCNALLY, B.M. MONGE-SANZ, J.J. MORCRETTE, B.K. PARK, C. PEUBEY, P. DE ROSNAY, C. TAVOLATO, J.N. THÉPAUT, F. VITART, 2011: The era-interim reanalysis: configuration and performance of the data assimilation system. – Quart. J. Roy. Meteor. Soc. **137**, 553–597, DOI: 10.1002/qj.828.

DJATH, B., J. SCHULZ-STELLENFLETH, 2019: Wind speed deficits downstream offshore wind parks – A new automised estimation technique based on satellite synthetic aperture radar data. – Meteorol. Z. **28**, 499–515, DOI: 10.1127/metz/2019/0992.

DJATH, B., J. SCHULZ-STELLENFLETH, B. CAÑADILLAS, 2018: Impact of atmospheric stability on X-band and C-band Synthetic Aperture Radar imagery of offshore windpark wakes. – J. Sustain. Renew. Energy **10**, DOI: 10.1063/1.5020437.

DJATH, B., J. SCHULZ-STELLENFLETH, B. CAÑADILLAS, 2022: Study of coastal effects relevant for offshore wind energy using spaceborne synthetic aperture radar (sar). – Remote Sens. **14**, DOI: 10.3390/rs14071688.

DONLON, C.J., M. MARTIN, J. STARK, J. ROBERTS-JONES, E. FIEDLER, W. WIMMER, 2012: The operational sea surface temperature and sea ice analysis (ostia) system. – Remote Sens. Env. **116**, 140–158, DOI: 10.1016/j.rse.2010.10.017. Advanced Along Track Scanning Radiometer(AATSR) Special Issue.

DÖRENKÄMPER, M., B.T. OLSEN, B. WITHA, A.N. HAHMANN, N.N. DAVIS, J. BARCONS, Y. EZBER, E. GARCÍA-BUSTAMANTE, J.F. GONZÁLEZ-ROUCO, J. NAVARRO, M. SASTRE-MARUGÁN, T. SĪLE, W. TREI, M. ŽAGAR, J. BADGER, J. GOTTSCHALL, J. SANZ RODRIGO, J. MANN, 2020: The making of the new european wind atlas – part 2: Production and evaluation. – Geosci. Model Dev. **13**, 5079–5102, DOI: 10.5194/gmd-13-5079-2020.

DRAXL, C., A. CLIFTON, B.M. HODGE, J. MCCAA, 2015: The wind integration national dataset (wind) toolkit. – Appl. Energy **151**, 355–366, DOI: 10.1016/j.apenergy.2015.03.121.

DÍAZ, H., C. GUEDES SOARES, 2020: Review of the current status, technology and future trends of offshore wind farms. – Ocean Engineer. **209**, 107381, DOI: 10.1016/j.oceaneng.2020.107381.

EMEIS, S., S. SIEDERSLEBEN, A. LAMPERT, A. PLATIS, J. BANGE, B. DJATH, J. SCHULZ-STELLENFLETH, T. NEUMANN, 2016: Exploring the wakes of large offshore wind farms. – J. Phys. Conf. Ser.**753**, 092014, DOI: 10.1088/1742-6596/753/9/092014.

FOREMAN, R.J., S. EMEIS, B. CAÑADILLAS, 2015: Half-order stable boundary-layer parametrization without the eddy viscosity approach for use in numerical weather prediction. – Bound.-Layer Meteor. **154**, 207–228.

GEBCO COMPILATION GROUP, 2020: GEBCO 2020 Grid.

GUALTIERI, G., 2021: Reliability of era5 reanalysis data for wind resource assessment: A comparison against tall towers. – Energies **14**, DOI: 10.3390/en14144169.

HAHMANN, A.N., C.L. VINCENT, A. PEÑA, J. LANGE, C.B. HASAGER, 2015: Wind climate estimation using wrf model output: method and model sensitivities over the sea. – Int. J. Climatol. **35**, 3422–3439, DOI: 10.1002/joc.4217.

HAHMANN, A.N., T. SĪLE, B. WITHA, N.N. DAVIS, M. DÖRENKÄMPER, Y. EZBER, E. GARCÍA-BUSTAMANTE, J.F. GONZÁLEZ-ROUCO, J. NAVARRO, B.T. OLSEN, S. SÖDERBERG, 2020: The making of the new european wind atlas – part 1: Model sensitivity. – Geosci. Model Develop. **13**, 5053–5078, DOI: 10.5194/gmd-13-5053-2020.

HASAGER, C.B., M. BADGER, A. PEÑA, X.G. LARSÉN, F. BINGÖL, 2011: SAR-based wind resource statistics in the Baltic Sea. – Remote Sens. **3**, 117–144.

HERSBACH, H., A. STOFFELEN, S. DE HAAN, 2007: An improved C-band scatterometer ocean geophysical model function: CMOD5. – J. Geophys. Res. Oceans **112**.

HERSBACH, H., B. BELL, P. BERRISFORD, S. HIRAHARA, A. HORÁNYI, J. MUÑOZ-SABATER, J. NICOLAS, C. PEUBEY, R. RADU, D. SCHEPERS, A. SIMMONS, C. SOCI, S. ABDALLA, X. ABELLAN, G. BALSAMO, P. BECHTOLD, G. BIAVATI, J. BIDLOT, M. BONAVITA, G. DE CHIARA, P. DAHLGREN, D. DEE, M. DIAMANTAKIS, R. DRAGANI, J. FLEMMING, R. FORBES, M. FUENTES, A. GEER, L. HAIMBERGER, S. HEALY, R.J. HOGAN, E. HÓLM, M. JANISKOVÁ, S. KEELEY, P. LALOYAUX, P. LOPEZ, C. LUPU, G. RADNOTI, P. DE ROSNAY,

Meteorol. Z. (Contrib. Atm. Sci.)
Early Access Article, 2023

B. Cañadillas et al.: Coastal horizontal wind speed gradients

21

I. Rozum, F. Vamborg, S. Villaume, J.N. Thépaut, 2020: The era5 global reanalysis. – Quart. J. Roy. Meteor. Soc. **146**, 1999–2049, DOI: 10.1002/qj.3803.

Johannessen, J.A., R.A. Shuchman, O.M. Johannessen, K.L. Davidson, D.R. Lyzenga, 1991: Synthetic aperture radar imaging of upper ocean circulation features and wind fronts. – J. Geophys. Res. Oceans **96**, 10411–10422.

Jourdier, B., 2020: Evaluation of era5, merra-2, cosmo-rea6, newa and arome to simulate wind power production over france. – Advan. Sci. Res. **17**, 63–77, DOI: 10.5194/asr-17-63-2020.

Källstrand, B., H. Bergström, J. Højstrup, A.S. Smedman, 2000: Mesoscale wind field modifications over the baltic sea. – Bound.-Layer Meteor. **95**, 161–188.

Kalverla, P.C., J.B. Duncan Jr., G.J. Steeneveld, A.A.M. Holtslag, 2019: Low-level jets over the north sea based on era5 and observations: together they do better. – Wind Energy Sci. **4**, 193–209, DOI: 10.5194/wes-4-193-2019.

Kibona, T.E., 2020: Application of wrf mesoscale model for prediction of wind energy resources in tanzania. – Scientific African **7**, e00302, DOI: 10.1016/j.sciaf.2020.e00302.

Lampert, A., K. Bärfuss, A. Platis, S. Siedersleben, B. Djath, B. Cañadillas, R. Hunger, R. Hankers, M. Bitter, T. Feuerle, H. Schulz, T. Rausch, M. Angermann, A. Schwithal, J. Bange, J. Schulz-Stellenfleth, T. Neumann, S. Emeis, 2020: In situ airborne measurements of atmospheric and sea surface parameters related to offshore wind parks in the german bight. – Earth Sys. Sci. Data **12**, 935–946, DOI: 10.5194/essd-12-935-2020.

Lapworth, A., 2005: The diurnal variation of the marine surface wind in an offshore flow. – Quart. J. Roy. Meteor. Soc. **131**, 2367–2387.

Leiding, T., B. Tinz, L. Gates, G. Rosenhagen, K. Herklotz, C. Senet, O. Outzen, A. Lindenthal, T. Neumann, R. Frühmann, F. Wilts, F. Bégué, P. Schwenk, D. Stein, I. Bastigkeit, B. Lange, S. Hagemann, S. Müller, J. Schwabe, 2016: Standardisierung und vergleichende Analyse der meteorologischen FINO-Messdaten (fino123). – Project report (0325508), Deutscher Wetterdienst (DWD), Bundesamt für Schifffahrt und Hydrographie Hamburg (BSH), UL International GmbH, DNV-GL, Fraunhofer IWES, WIND-consult.

Li, X., S. Lehner, 2013: Observation of TerraSAR-X for studies on offshore wind turbine wake in near and far fields. – Selected Topics in Applied Earth Observations and Remote Sensing, IEEE Journal **6**, 1757–1768, DOI: 10.1109/JSTARS.2013.2263577.

Meyer, P., J. Gottschall, 2022: How do newa and era5 compare for assessing offshore wind resources and wind farm siting conditions? – J. Phys. Conf. Ser. **2151**, 012009, DOI: 10.1088/1742-6596/2151/1/012009.

Olauson, J., 2018: Era5: The new champion of wind power modelling?. – Renew. Energy **126**, 322–331, DOI: 10.1016/j.renene.2018.03.056.

Peter, H., A. J'aggi, J. Fernández, D. Escobar, F. Ayuga, D. Arnold, M. Wermuth, S. Hackel, M. Otten, W. Simons, P. Visser, U. Hugentobler, P. Féménias, 2017: Sentinel-1a – first precise orbit determination results. – Advan. Space Res. **60**, 879–892, DOI: 10.1016/j.asr.2017.05.034.

Platis, A., M. Hundhausen, A. Lampert, S. Emeis, J. Bange, 2022: The role of atmospheric stability and turbulence in offshore wind-farm wakes in the german bight. – Bound.-Layer Meteor. 1573–1472, DOI: 10.1007/s10546-021-00668-4.

Podein, P., B. Tinz, R. Blender, T. Detels, 2022: Reconstruction of annual mean wind speed statistics at 100 m height of FINO1 and FINO2 masts with reanalyses and the geostrophic wind. – Meteorol. Z. **31**, 89–100, DOI: 10.1127/metz/2021/1090.

Portabella, M., A. Stoffelen, J.A. Johannessen, 2002: Toward an optimal inversion method for synthetic aperture radar wind retrieval. – J. Geophys. Res. Oceans **107**, 1–1–1–13, DOI: 10.1029/2001JC000925.

Pronk, V., N. Bodini, M. Optis, J.K. Lundquist, P. Moriarty, C. Draxl, A. Purkayastha, E. Young, 2022: Can reanalysis products outperform mesoscale numerical weather prediction models in modeling the wind resource in simple terrain? – Wind Energy Sci. **7**, 487–504, DOI: 10.5194/wes-7-487-2022.

Pryor, S.C., R.J. Barthelmie, 1998: Analysis of the effect of the coastal discontinuity on near-surface flow. – Annales Geophysicae **16**, 882–888, DOI: 10.1007/s00585-998-0882-3.

Pryor, S.C., T.J. Shepherd, R.J. Barthelmie, A.N. Hahmann, P. Volker, 2019: Wind farm wakes simulated using WRF. – J. Phys. Conf. Ser. **1256**, 012025, DOI: 10.1088/1742-6596/1256/1/012025.

Rausch, T., B. Cañadillas, O. Hampel, T. Simsek, Y.B. Tayfun, T. Neumann, S. Siedersleben, A. Lampert, 2022: Wind lidar and radiosonde measurements of low-level jets in coastal areas of the german bight. – Atmosphere **13**, DOI: 10.3390/atmos13050839.

Santos, J., Y. Sakagami, R. Haas, J. Passos, M. Machuca, W. Correa Radunz, E. Dias, M. Lima, 2019: Wind speed evaluation of MERRA-2, ERA-interim and ERA-5 reanalysis data at a wind farm located in Brazil. – ISES Solar World Congress 2019/IEA SHC International Conference on Solar Heating and Cooling for Buildings and Industry 2019, published online, DOI: 10.18086/swc.2019.45.10.

Schulz-Stellenfleth, J., S. Emeis, M. Dörenkämper, J. Bange, B. Cañadillas, T. Neumann, J. Schneemann, I. Weber, K. zum Berge, A. Platis, B. Djath, J. Gottschall, L. Vollmer, T. Rausch, M. Barekzai, J. Hammel, G. Steinfeld, A. Lampert, 2022: Coastal impacts on offshore wind farms – a review focussing on the german bight area. – Meteorol. Z. **31**, 289–315, DOI: 10.1127/metz/2022/1109. 12.11.11; LK 01.

Shamshirband, S., A. Mosavi, N. Nabipour, K.w. Chau, 2020: Application of ERA5 and MENA simulations to predict offshore wind energy potential. – Atmos. Oceanic Phys., published online, DOI: 10.48550/ARXIV.2002.10022.

Sheridan, L.M., R. Krishnamurthy, B.J. Gaudet, 2021: Assessment of model hub height wind speed performance using DOE Lidar Buoy data. – Technical report, Pacific Northwest National Lab.(PNNL), Richland, WA (United States).

Shimada, S., Y. Takeyama, T. Kogaki, T. Ohsawa, S. Nakamura, 2018: Investigation of the fetch effect using onshore and offshore vertical lidar devices. – Remote Sens. **10**, 1408, DOI: 10.3390/rs10091408.

Siedersleben, S.K., A. Platis, J.K. Lundquist, A. Lampert, K. Bärfuss, B. Cañadillas, B. Djath, J. Schulz-Stellenfleth, J. Bange, T. Neumann, S. Emeis, 2018: Evaluation of a wind farm parametrization for mesoscale atmospheric flow models with aircraft measurements. – Meteorol. Z. **27**, 401–415, DOI: 10.1127/metz/2018/0900.

Skamarock, W., J. Klemp, J. Dudhia, D. Gill, Z. Liu, J. Berner, W. Wang, J. Power, M. Duda, D. Barker, X.Y. Huang, 2019: A description of the advanced research WRF version 3. – Technical Report, 162 pages NCAR/TN-556+STR, NCAR – National Center for Atmospheric Research, Boulder, Colorado, USA, DOI: 10.5065/1dfh-6p97.

Skyllingstad, E., R. Samelson, L. Mahrt, P. Barbour, 2005: A numerical modeling study of warm offshore flow over cool water. – Mon. Wea. Rev. **133**, 345–361, DOI: 10.1175/MWR-2845.1.

SMEDMAN, A.S., 1991: Occurrence of roll circulations in a shallow boundary layer. – Bound.-Layer Meteor. **57**, 343–358, DOI: 10.1007/BF00120053.

SMEDMAN, A.S., H. ULF, B. HANS, 1996: Low level jets – a decisive factor for off-shore wind energy siting in the baltic sea. – Wind Engineer. **20**, 137–47.

SOARES, P.M.M., D.C.A. LIMA, M. NOGUEIRA, 2020: Global offshore wind energy resources using the new ERA-5 reanalysis. – Env. Res. Lett. **15**, 1040a2, DOI: 10.1088/1748-9326/abb10d.

SOLER-BIENTZ, R., S. WATSON, 2016: Preliminary assessment of the variability of uk offshore wind speed as a function of distance to the coast. – J. Phys. Conf. Ser. **749**, 012004, DOI: 10.1088/1742-6596/749/1/012004.

STULL, R.B., 1988: An Introduction to Boundary Layer Meteorology. – Kluwer Academic Publishers, Dordrecht.

TAYLOR, P., 1969: On wind and shear stress profiles above a change in surface roughness. – Quart. J. Roy. Meteor. Soc. **95**, 77–91.

THOMAS, S.R., S. NICOLAU, O. MARTÍNEZ-ALVARADO, D.J. DREW, H.C. BLOOMFIELD, 2021: How well do atmospheric reanalyses reproduce observed winds in coastal regions of Mexico? – Meteor. Appl. **28**, e2023, DOI: 10.1002/met.2023.

TORRES, R., P. SNOEIJ, D. GEUDTNER, D. BIBBY, M. DAVIDSON, E. ATTEMA, P. POTIN, B. ROMMEN, N. FLOURY, M. BROWN, OTHERS, 2012: GMES Sentinel-1 mission. – Remote Sens. Env. **120**, 9–24.

VERHOEF, A., M. PORTABELLA, A. STOFFELEN, H. HERSBACH, 2008: CMOD5. n-the CMOD5 GMF for neutral winds. – Technical Report SAF/OSI/CDOP/KNMI/TEC/TN/3, 165, KNMI, De Bilt, Netherlands.

WRF USERS PAGE, 2020: WRF model physics options and references. – WRF USers page, https://www2.mmm.ucar.edu/wrf/users/, last accessed: 13.07.2020.

ZHENG, C.W., NIU Z. XIAO, HUA Y. PENG, YIN C. LI, BO Z. DU, 2018: Rezoning global offshore wind energy resources. – Renew. Energy **129**, 1–11, DOI: 10.1016/j.renene.2018.05.090.

ZÄNGL, G., D. REINERT, P. RÍPODAS, M. BALDAUF, 2015: The ICON (ICOsahedral Non-hydrostatic) modelling framework of DWD and MPI-M: Description of the non-hydrostatic dynamical core. – Quart. J. Roy. Meteor. Soc. **141**, 563–579, DOI: 10.1002/qj.2378. _eprint: https://rmets.onlinelibrary.wiley.com/doi/pdf/10.1002/qj.2378.